Materials Research Express

Check for updates

OPEN ACCESS

RECEIVED
14 July 2026

REVISED
20 September 2026

ACCEPTED FOR PUBLICATION
5 October 2026

PUBLISHED
16 October 2026

Original content from this work may be used under the terms of the Creative Commons Attribution 4.0 licence.

Any further distribution of this work must maintain attribution to the author(s) and the title of the work, journal citation and DOI.

PAPER

Post-aging-induced microstructural, mechanical, and ductile fracture characteristics of 6082-T6 aluminum alloy

Mehmet Okan Kabakçı[1], Onur Cavusoglu[1,*], Ömer Şahin[2], Oktay Cavusoglu[3], Şaziye Efendioğlu Ünal[4] and Anıl Ozdemir[5]

[1] Gazi University, Faculty of Technology, Department of Manufacturing Engineering, 06560 Ankara, Türkiye
[2] Gazi University, Faculty of Technology, Department of Metallurgical and Materials Engineering, 06560 Ankara, Türkiye
[3] Düzce University, Faculty of Engineering, Department of Mechanical Engineering, Düzce 81620, Türkiye
[4] TOFAŞ, Turkish Automobile Factory, Bursa 16110, Türkiye
[5] Gazi University, Faculty of Technology, Department of Civil Engineering, 06560 Ankara, Türkiye
[*] Author to whom any correspondence should be addressed.

E-mail: onurcavusoglu@gazi.edu.tr

Keywords: 6082-T6, aging, digital image correlation (DIC), mechanical properties, fracture, energy absorption

Abstract

In this study, the effects of post-aging conditions on the mechanical properties, deformation behavior, and fracture characteristics of 6082-T6 aluminum alloy sheets were investigated, using tensile testing supported by DIC. Post-aging treatments were performed at 100 °C, 200 °C, 300 °C, and 400 °C, with holding times of 30, 60, and 90 min at each temperature. The following parameters were determined from the tensile tests: yield strength, tensile strength, strain-hardening exponent, uniform elongation, total elongation, and energy absorption capacity. Microstructural and fracture analyses were performed using optical microscopy and scanning electron microscopy, while x-ray diffraction was used to evaluate phase-related structural changes. Hardness variations were assessed by Vickers hardness testing. Fracture-surface dimple morphologies were quantitatively evaluated using average dimple diameter and standard deviation values to assess the temperature- and time-dependent variation in fracture behavior. The results showed that aging at 200 °C for 60 min provided a highly favorable strength–ductility balance and was identified as the most efficient processing condition in terms of the combined mechanical response, with a yield strength of approximately 289 MPa, tensile strength of about 400 MPa, uniform elongation of 15.9%, total elongation of 17.4%, hardness of 115.6 HV, and energy absorption of 61.36 MJ m^{-3}. At 300 °C–400 °C, pronounced overaging occurred as precipitate coarsening reduced the effectiveness of precipitation strengthening, leading to significant degradation in mechanical performance. The strain-hardening response and energy absorption capacity were found to be strongly dependent on the aging condition. The results indicate a transition from relatively homogeneous deformation to strain-localized behavior as aging temperature increases, consistent with reduced deformation stability at elevated temperatures. Overall, these findings demonstrate that controlled post-aging can tailor the strength–ductility balance and fracture response of AA6082-T6 sheets.

1. Introduction

The aluminum alloy plays an important role in today's industry because of its many favorable characteristics, such as low weight, high strength, excellent workability, and corrosion resistance. Aluminum alloys have been utilized in a variety of applications, particularly in automotive and aerospace engineering [1–4]. Aluminum alloys have emerged as a compelling solution to address concerns regarding energy conservation and sustainability. These alloys serve as a viable substitute for conventional materials, such as steel, due to their reduced energy requirements and diminished carbon footprint. Aluminum alloys are distinguished by their exceptional recyclability, which further enhances their environmental sustainability [5]. Improvements of mechanical and thermal properties through innovative

© 2026 The Author(s). Published by IOP Publishing Ltd

manufacturing processes and studies related to alloy development remain at the core of such endeavors. The goal of these endeavors is optimization of material properties [6–8]. Aging of aluminum alloy sheets is a heat treatment process that seeks to improve the properties of the alloy through controlling the microstructure. The process at hand seeks to maximize the properties of the alloy for efficient and durable use in industrial settings. This is done through balancing ductility and increasing the alloy's strength [9–13]. The aging process facilitates the development of an optimal microstructure that enhances strength through mechanisms such as precipitation hardening. The precipitation evolution, which influences material performance, is contingent upon factors such as aging temperature, duration, and alloy composition [14–16].

The interactions among aging conditions, precipitation behavior, microstructural evolution, and mechanical properties of aluminum alloys have been extensively investigated in the literature. Chen *et al* artificially aged 6061 aluminum alloy at 160 °C, 180 °C, and 200 °C for up to 48 h. According to their study findings, the maximum strength was obtained at the aging temperature of 200 °C for six hours. During aging, the Mg_2Si nanoparticles were precipitated homogeneously in the matrix, which caused strength improvement [17]. Yin *et al* conducted experiments on artificial aging of 6151 aluminum alloy at temperatures of 160 °C, 180 °C, and 200 °C for 20 min, 30 min, and 40 min, respectively. Their results showed that the maximum mechanical properties are obtained at 200 °C for 40 min [18]. Görtan and Yüksel conducted a study to ascertain the effect of temperature and aging time on the mechanical properties of the 6082-aluminum alloy. The experimental findings indicate that elevated temperatures, particularly those above 200 °C, result in improved mechanical properties when used for short periods of time [19]. Hu *et al* artificially aged 6082 aluminum alloys at a temperature of 180 °C for varying durations: 2, 4, 6, and 8 h, respectively. The present study investigated the influence of aging duration on material hardness. To achieve this objective, a thorough analysis of the microstructural precipitation mechanisms was performed, which revealed that prolonged aging processes lead to a degradation of the mechanical properties [20]. The effects of aging time and temperature were studied by Liu *et al* using 6005 A aluminum alloy at temperatures of 155 °C, 175 °C, and 195 °C for eight hours. It was found that the best mechanical properties can be obtained when the aging temperature is set at 175 °C and the aging time is eight hours. During such an aging process, the strength gain is due to the optimized formation of Guinier–Preston zones and β'' phases [21]. The mechanical property optimization through aging temperature (160 °C, 170 °C, 180 °C, 190 °C) and aging time (4, 6, 8, 10 h) of AA6063 aluminum alloy was studied by Sui Zihao *et al*. According to the findings of the study, the optimal aging parameters were identified as an aging temperature of 170 °C for a duration of 8 h. Aging at a temperature maintained below 170 °C resulted in a decrease in precipitation and, consequently, a decrease in mechanical properties. However, aging temperatures above 170 °C accelerated the transformation of β'' precipitates into β' phases [22]. Xia *et al* performed artificial aging on 6082 aluminum alloys for eight hours at 180 °C following solution treatment. This improved the mechanical properties of the aluminum alloy. Elongation was found to decrease during this process [23]. An investigation into the use of artificial aging in 6022 aluminum alloy was conducted by Okayasu and Okawa. This experiment involved several temperatures, namely, 150 °C, 170 °C, and 200 °C, as well as aging times from 0 to 13 h after the hot stamping process. It is observed that the ideal condition for maximizing hardness and strength while minimizing elongation is achieved by artificial aging at 170 °C for 4 h [24]. In the study by Arslankaya, the influence of aging treatments on the mechanical properties of 6061 aluminum alloy was evaluated at temperatures between 170 °C and 200 °C for times ranging from two to 12 h. According to the research, mechanical properties are at their best when aging is conducted at 180 °C for 8 h because of the proper size and distribution of the precipitates. In addition, increased mechanical strength has been observed when aging occurs at higher temperatures or times [25]. As reported by Chen *et al*, the maximum hardness and tensile strength of an Al-0.50 Mg-1.15Si alloy can be achieved by aging at 175 °C for 2–60 h. However, excessive aging leads to deterioration of the alloy properties due to the conversion of β'' phases to β' phases [26]. The effect of age hardening on AA7075-T6 was studied by Österreicher *et al*, who demonstrated that GP zones, which form during pre-aging at 120 °C, are instrumental in the nucleation of the η' phase during post-forming paint baking. The optimal combination of tensile strength and elongation was observed within the temperature range of 180 °C–210 °C. However, aging at 250 °C resulted in suboptimal mechanical properties, attributable to coarsening of precipitates [27]. Gong *et al* investigated the artificial aging characteristics of 7075 aluminum alloy through aging processes conducted at 120 °C with various aging times. The aging times were categorized as 8 h (Underaged, UA), 24 h (Peak-aged, PA), and 48 h (Overaged, OA). The results of the study indicate a positive correlation between the initial precipitate density and the aging time [28]. Xia *et al* studied the mechanical behavior and microstructure evolution of 6082 aluminum alloy subjected to different aging processes.

Table 1. Chemical composition of AA6082-T6 (wt %).

Material	Fe	Si	Cu	Mn	Mg	Zn	Cr	Other	Al
6082-T6	0.37	0.9	0.1	0.46	0.7	0.1	0.02	0.04	Balance

Aging at a low temperature (180 °C for 8 h) would be effective when strength is the primary requirement. A shorter treatment at an intermediate temperature (280 °C for 0.5 h) was reported to provide a desirable balance of strength and ductility. In certain applications, an optimal level of ductility has been observed when the material is subjected to a high-temperature aging process for a brief duration (330 °C for 0.5 h) [29].

Previous studies demonstrate that the mechanical response of precipitation-hardenable aluminum alloys is governed by the combined effects of aging temperature and time rather than by either parameter independently. Lower aging temperatures generally require longer holding times to approach peak strength, whereas increasing the aging temperature accelerates precipitation kinetics and shortens the time required to reach the peak-aged condition. Prolonged exposure may promote precipitate coarsening and the transformation of metastable strengthening phases, leading to over-aging and a corresponding change in the strength–ductility balance. Differences in the reported peak-aging conditions can be attributed to variations in alloy composition, solute content, Mg/Si ratio, initial temper, prior thermomechanical history, solution-treatment and quenching conditions, and natural or pre-aging history. These factors influence precipitation kinetics and phase stability and therefore explain why different studies report different peak-aging conditions, even among alloys belonging to the same precipitation-hardening system. In addition, the criterion used to define the optimum condition, such as hardness, yield strength, tensile strength, or the strength–ductility balance, may also lead to different reported optimum conditions. Therefore, optimum aging parameters reported for different aluminum alloys, or even for the same alloy subjected to different processing histories, are not directly interchangeable. Although precipitation sequences, precipitate morphology and distribution, and dislocation–precipitate interactions have been extensively investigated, the coupled relationship between post-aging-induced strain localization and fracture-surface morphology in AA6082-T6 sheets has received comparatively limited attention.

In the present study, the post-aging temperature range was intentionally extended beyond the conventional artificial-aging regime. While 100 °C–200 °C represents re-aging/post-aging conditions, 300 °C–400 °C was selected to examine the transition from precipitation-controlled strengthening to thermally induced softening associated with precipitate coarsening, transformation, or partial dissolution.

This study addresses this gap by examining the mechanical properties, together with deformation behavior and fracture characteristics of AA6082-T6 aluminum alloy under different post-aging conditions. This study provides a temperature–time dependent deformation–fracture response map linking post-aging temperature–time combinations to (i) tensile response and deformation behavior and (ii) the associated fracture-surface morphology in AA6082-T6 sheets. The novelty of this work lies in the combined evaluation of deformation behavior and fracture morphology through strain analysis and quantitative dimple characterization, providing insight into the relationship between deformation heterogeneity and fracture surface evolution under different post-aging conditions in AA6082-T6 alloy. Optical microscopy (OM) observations and x-ray diffraction (XRD) trends are used to support the interpretation of the post-aging-induced microstructural changes qualitatively and to identify the condition that provides the most balanced mechanical performance.

2. Material and experimental study

2.1. Material

The experimental specimens were produced from 3 mm-thick 6082-T6 sheet material in accordance with ASTM E8/E8M and were cut parallel to the rolling direction using the water-jet cutting method. The gauge length and gauge width of the tensile specimens were 50 mm and 25 mm, respectively. The chemical composition of the 6082-T6 sheet material is presented in table 1.

2.2. Experimental study

The experimental specimens were aged at temperatures of 100 °C, 200 °C, 300 °C, and 400 °C using a proportional-integral-derivative (PID) controlled resistance furnace. Within the scope of this study, aging processes of 30 min, 60 min, and 90 min were applied to 3 mm thick 6082 aluminum alloy test specimens to observe the relationship between aging time and the resulting properties. In the aging process,

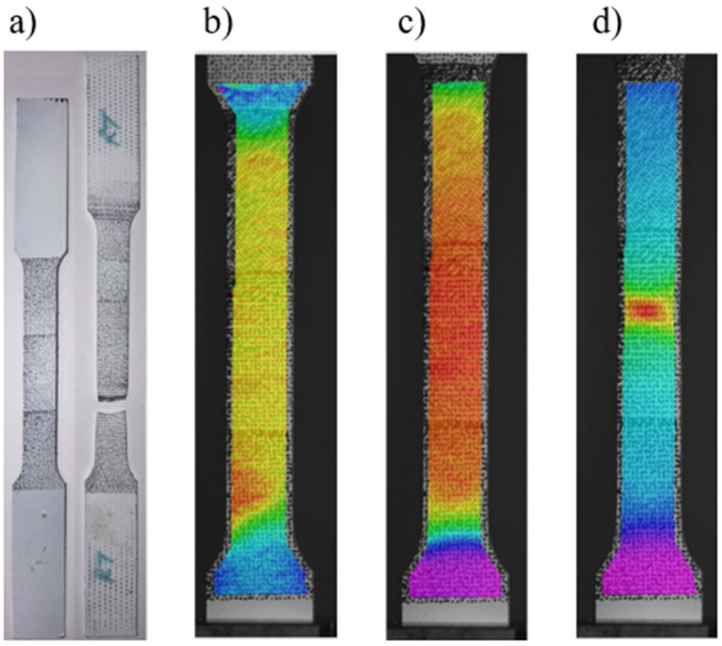


Figure 1. (a) Speckled tensile specimen; representative DIC strain maps at (b) early plastic deformation, (c) necking onset, and (d) near-fracture localization.

the experimental specimens placed inside the furnace were processed by adjusting the heating regime, holding time, and door opening time parameters from the PID control unit. The experimental specimens were brought to the specified aging temperature at a heating rate of 10 °C min^{-1} and held at a constant temperature for the specified holding times. After the holding time, specimens were air-cooled to room temperature.

Accordingly, the aging treatments at 300 °C–400 °C are not considered conventional artificial-aging conditions but rather high-temperature post-aging thermal exposures. These conditions were included to evaluate the response of AA6082-T6 over an extended thermal range, including the transition toward overaging and thermally induced softening.

After the aging process, the mechanical properties were examined using uniaxial tensile tests performed on an Instron 8503 tensile-compression testing machine with a capacity of 500 kN. The experimental data were collected using a digital image correlation (DIC) system to monitor strain evolution during tensile testing and to evaluate the evolution of full-field strain distribution and strain localization during tensile deformation. Uniaxial tensile tests were performed in accordance with ASTM E8/E8M at a strain rate of 0.0083 s^{-1}. Each tensile test was performed at least three times under identical conditions, and the reported values represent the average of the measurements. Standard deviations were calculated to evaluate the variability of the experimental data. The specimens' surfaces were wet prepared for DIC measurements before tensile testing. Initially, the surfaces of the AA6082-T6 aluminum sheet specimens were cleaned, followed by the application of a thin coating of matte white paint. Random black speckle patterns were subsequently applied to the sample using a spraying approach to establish adequate grayscale contrast between the speckles and the background surface. The mean speckle size was calibrated to range from 3 to 5 pixels. The data collected simultaneously from the DIC system and the testing machine were synchronized and processed to obtain the final experimental results. Instead of displacement gauges, a stereo DIC system consisting of two Daheng cameras (ME2P-1230-23U3M) equipped with 50 mm Kowa LM lenses was employed. Image acquisition and displacement calculations were performed using MatchID software, with a subset size of 29 × 29 pixels, selected in accordance with the speckle size and imaging resolution. Figure 1 displays the test specimens and speckle patterns.

To investigate the effects of aging temperature and holding times on the microstructure of 6082-T6 sheet metal, the microstructures of the experimental specimens were examined by OM using a Leica DMI 5000 M microscope. Phase analysis was performed by XRD to evaluate aging-induced structural changes. Test specimens were prepared for each aging condition, with the rolling direction used as a reference for precise cutting. The specimens were subsequently prepared for metallographic analysis by grinding and polishing. Following polishing, the specimens were cleansed and etched for 30 s with

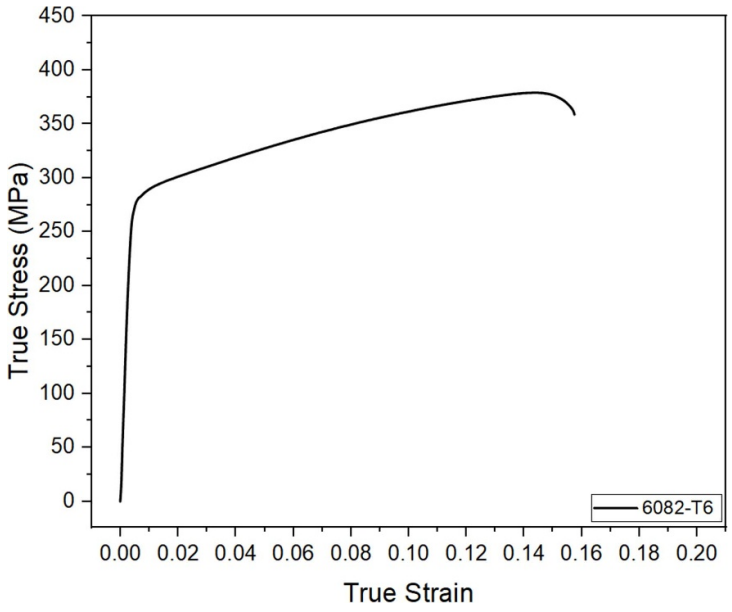


Figure 2. Experimentally obtained baseline true stress–true strain curve of the as-received AA6082-T6 alloy.

Keller's reagent (1 ml HF, 1.5 ml HCl, 2.5 ml HNO_3, and 95 ml H_2O). The fracture surfaces of the specimens were analyzed with a JEOL JSM-6060LV scanning electron microscopy (SEM), and the impact of the aging process on fracture behavior was assessed. The impact of heat treatment on the hardness of the 6082-T6 sheet material was assessed by Vickers hardness measurements performed in accordance with ASTM E384. An Vickers hardness (HV5) load was applied using an Instron–Wolpert Diatestor 7551 tester with a dwell time of 10 s, and at least five measurements were performed for each condition to ensure repeatability.

3. Results and discussion

As a result of this study, based on experimental data and microstructural examinations, the mechanical and microstructural properties of 6082-T6 aluminum alloy are presented after heat treatments applied at different post-aging temperatures (100 °C, 200 °C, 300 °C, and 400 °C) with holding times of 30, 60, and 90 min. From tensile curves obtained from tensile tests supported by DIC, the effects of post-aging conditions on the material were comprehensively evaluated by assessing yield and tensile strength, elongation capability, work hardening behavior, and energy absorption values, together with microstructural and fracture-surface observations obtained by OM, SEM, and XRD.

As illustrated in figure 2, the true stress-true strain curve for the as-received T6 condition is shown. The as-received (T6) condition exhibits a yield strength of 282.6 MPa, an ultimate tensile strength (UTS) of 379.1 MPa, and a total elongation of 15.73%. The true stress and true strain values were calculated using the standard constant-volume conversion formulations. While this conventional conversion is strictly valid only up to the onset of necking, the curves in this study are plotted up to fracture to visualize the macroscopic deformation behavior and to allow for the comparative calculation of energy absorption per unit volume (*Ev*). Therefore, the data points beyond uniform elongation represent apparent (nominal) true stress values without localized cross-sectional area correction.

Figures 3(a) and 3(b) show the stress–strain curves of specimens subjected to post-aging treatment at 100 °C and 200 °C for 30, 60, and 90 min, respectively. After aging at 100 °C, yield strength shows minor fluctuations around the T6 value (slight increase or slight decrease depending on holding time), while ductility is largely preserved. At 200 °C, especially after 60 min of processing, the maximum true stress reaches approximately 400 MPa, while the elongation capability is largely preserved. This response is consistent with strengthening by fine Mg–Si-type precipitates expected under peak-aging conditions, which restrict dislocation motion and increase strength. In figure 3(c), after the processes carried out at 300 °C, a significant decrease in strength values was observed. Specifically, after 90 min of aging, the maximum value of true stress reaches approximately 240 MPa, and the ductility properties of the specimen experience a decrease. The cause of this phenomenon can be attributed

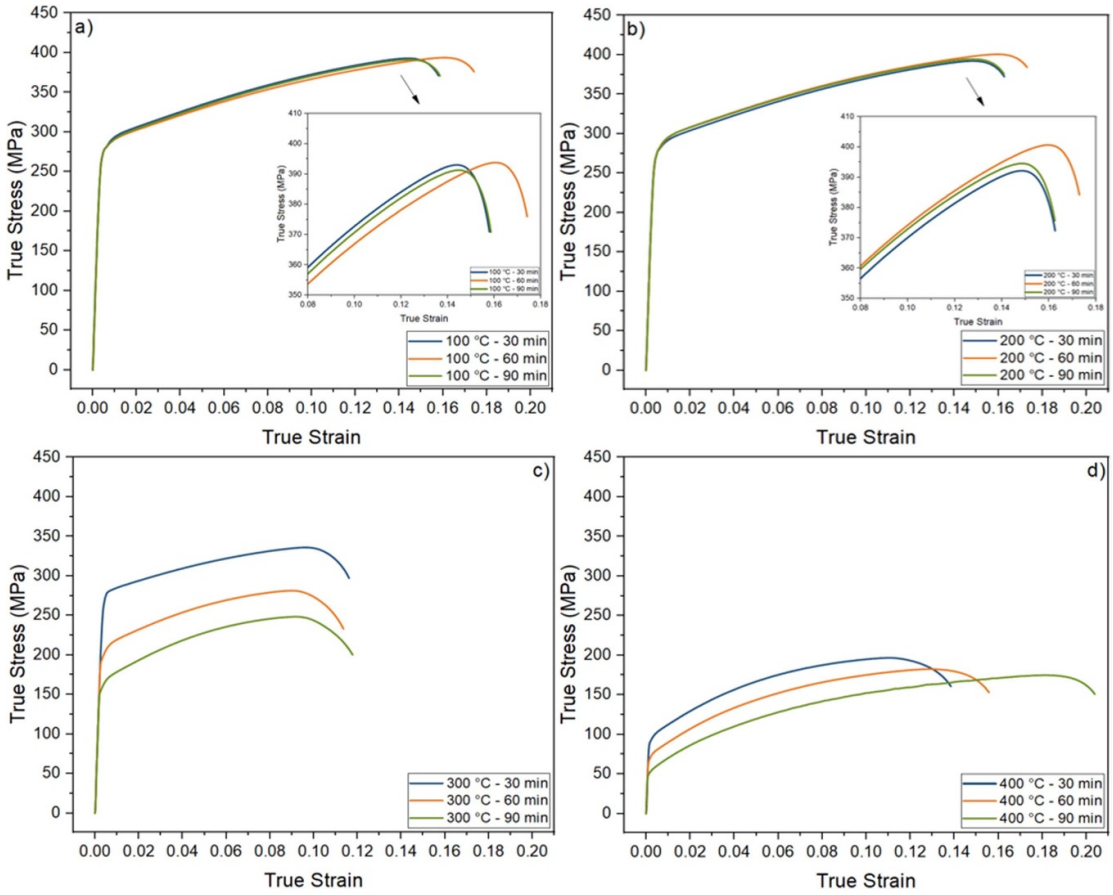


Figure 3. True stress–true strain curves of AA6082-T6 after post-aging at: (a) 100 °C, (b) 200 °C, (c) 300 °C, and (d) 400 °C for different holding times.

to two primary factors. First, the significant reduction in strength during over-aging is consistent with the loss of coherency as the highly coherent β'' precipitates transform into semi-coherent β' phases. During this transformation, the strengthening precipitates coarsen, become unevenly distributed, and their number density decreases, which significantly relaxes the three-dimensional coherent strain fields that obstruct dislocation motion [30, 31]. Second, due to this precipitate coarsening and increased inter-particle spacing, the Orowan bypassing mechanism becomes predominant rather than particle shearing [32]. The effect is high strength after short-time treatment, which lasts about 30 min. The effect of prolonged aging becomes negative during advanced aging. Figure 3(d) illustrates the effect of post-aging at 400 °C. The strength diminishes around 400 °C, and elongation exhibits non-linear behavior. Following 90 min of treatment, elongation increases due to the breakdown of precipitates. Thus, there seems to be a tendency towards developing a soft matrix rather than decreasing the overall deformability capability. Precipitates are highly incoherent at this temperature, and the fine precipitate content that strengthens the matrix is significantly reduced, leading to low strength values [33, 34].

Regarding the 6082-T6 aluminum alloy, there are reports that the strengthening effect is achieved at lower temperatures from 100 °C–200 °C without sacrificing its ductility [17–20]. However, at 300 °C, both ductility and strength have significantly reduced due to precipitation coarsening and coherency loss. An increase to 400 °C in the aging temperature results in a significant reduction in strength; however, this is accompanied by an enhancement in elongation due to matrix softening. Overall, post-aging at 200 °C (for 60 min) provides the best strength–ductility balance for industrial applications. High temperatures and long-term processes, however, negatively affect the material's performance [35, 36].

The effect of changing post-aging temperature and time on the yield strength of 6082-T6 aluminum alloy is indicated in figure 4. The initial yield strength of the material under the T6 condition is around 282.6 MPa. It has been observed that the yield strength stays almost constant between temperatures of 100 and 200 °C; however, there is a significant decrease in the range of 300–400 °C. This is particularly noticeable over longer periods of time, according to the conditions present during the post-aging process [37].

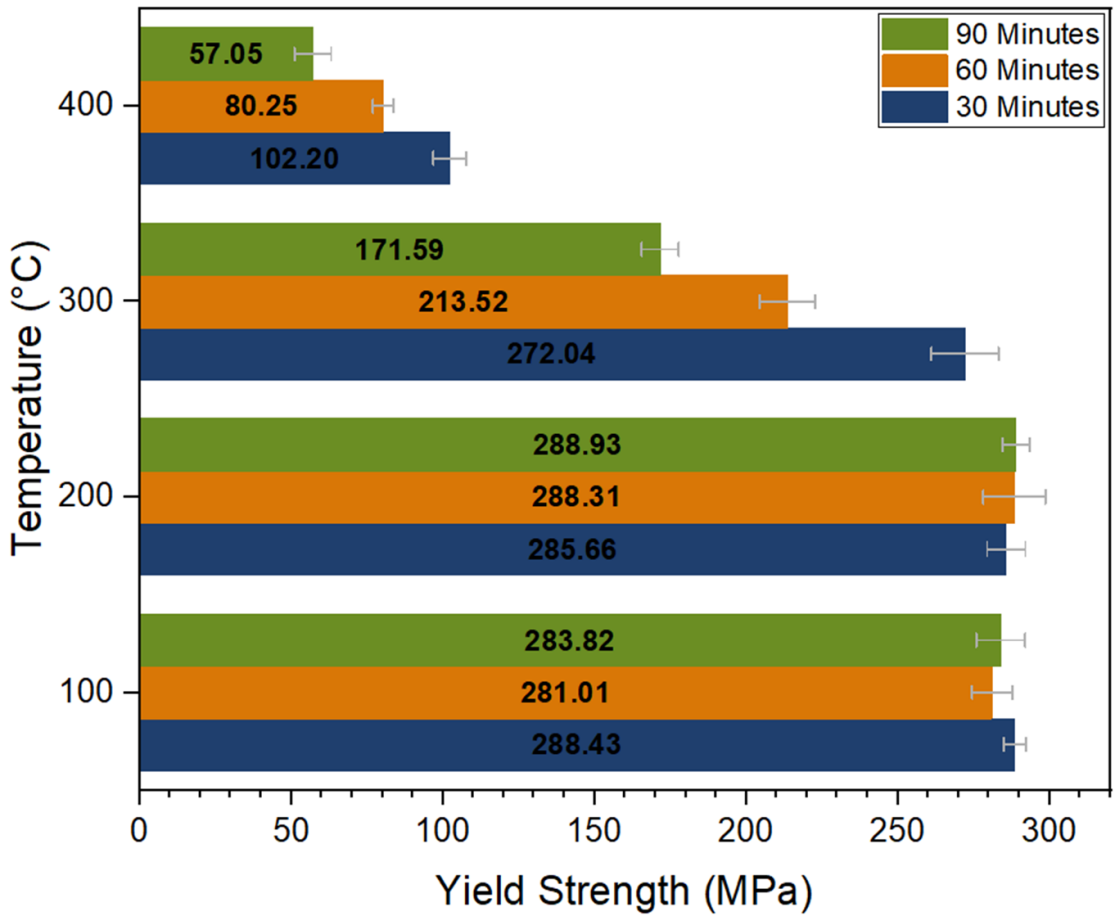


Figure 4. Effect of post-aging temperature and time on yield strength.

The yield strengths obtained after aging processes applied at 100 °C were measured as 288.43 MPa, 281.01 MPa, and 283.82 MPa for durations of 30, 60, and 90 min, respectively. It has been determined that these values are quite close to the initial strength under T6 conditions. Previous studies indicate that limited diffusion at low temperatures favors early-stage clustering and precipitation, including GP-zone formation and β''-related structures, while enhanced precipitate–matrix coherency can impede dislocation motion and thereby contribute to strength retention [38–40]. Aging at 200 °C resulted in the highest values for yield strength, which were 285.66 MPa after 30 min, 288.31 MPa after 60 min, and 288.93 MPa after 90 min. Considering the standard deviations, the marginal difference of 0.62 MPa between the 60- and 90 min treatments is small relative to the experimental scatter, meaning that the material reaches a strength plateau after 60 min. This yield strength response is consistent with a peak-aged condition, which is commonly associated with fine coherent β'' precipitates that can provide effective resistance to dislocation motion [41, 42]. Therefore, it is understood that short and medium-term aging at 200 °C provides optimal effects in terms of precipitation hardening. After aging at 300 °C for 30 min, the yield strength is 272.04 MPa, showing only a slight decrease compared to the T6 condition. However, it was observed that it decreased to 213.52 MPa in 60 min and to 171.59 MPa in 90 min. This reduction may be related to precipitate coarsening, increased precipitate size and spacing, and changes in precipitate–matrix coherency, which are commonly associated with over-aging in Al–Mg–Si alloys. These changes can reduce the effectiveness of precipitates as barriers to dislocation motion, thereby contributing to lower yield strength. Aging treatments performed at 400 °C were the most detrimental to yield strength, with values of 102.20 MPa, 80.25 MPa, and 57.05 MPa after aging for 30, 60, and 90 min, respectively. The pronounced strength reduction at this temperature is consistent with severe over-aging and thermally induced changes in the precipitation state, including precipitate coarsening and dissolution, as reported in the literature [43, 44].

The correlation between UTS and aging treatment temperature–time combination for 6082-T6 aluminum alloy is depicted in figure 5. The UTS of the received alloy in the T6 condition is found to be about 379.05 MPa. For samples aged at 100 °C for 30, 60, and 90 min, the UTS value is 393.02 MPa, 393.79 MPa, and 391.31 MPa, respectively. All these results indicate a close approximation to the

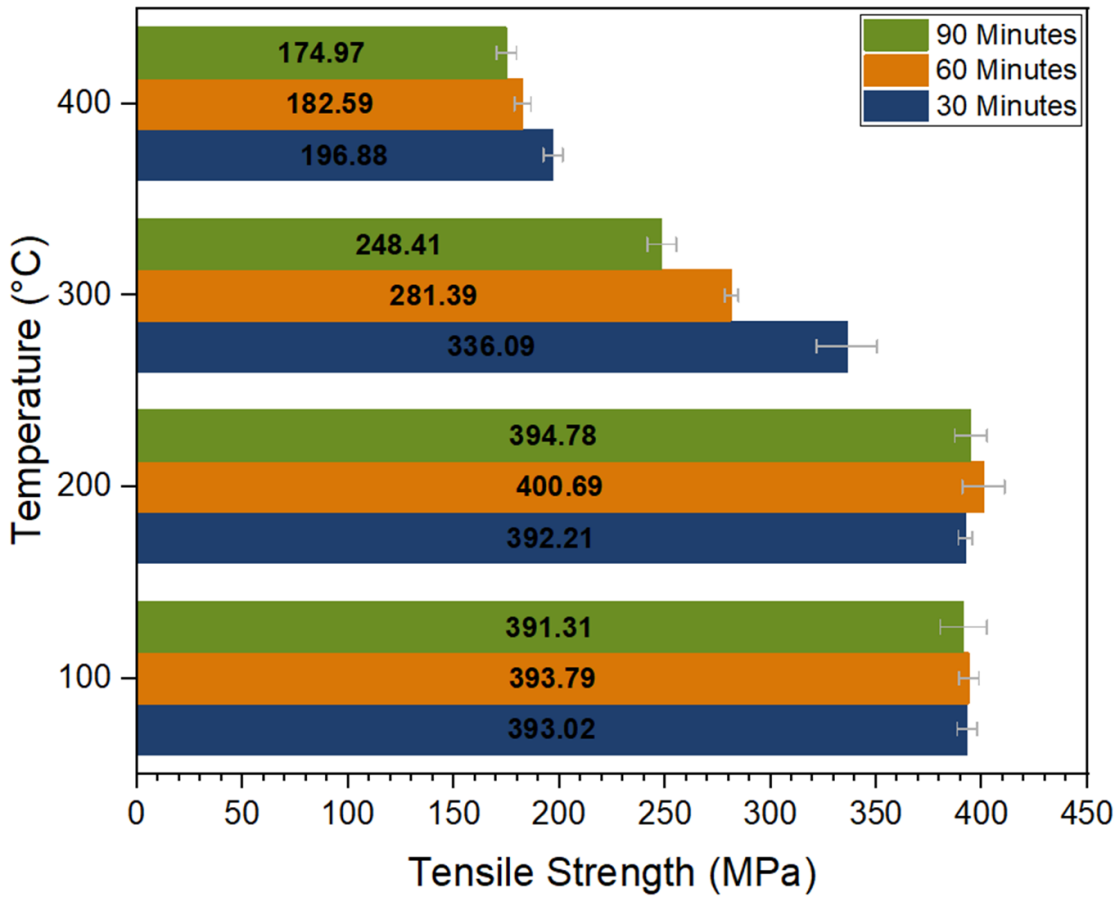


Figure 5. Tensile strength response of AA6082-T6 under different post-aging conditions.

T6 condition, consistent with the limited precipitation evolution reported during short-term aging at 100 °C, where nanoscale clusters initially dominate and β''-related structures develop only with further aging [38]. At 200 °C, tensile strength values of 392.21 MPa in 30 min, 400.69 MPa in 60 min, and 394.78 MPa in 90 min were obtained. This tensile strength response is consistent with a peak-aged condition, in which fine coherent β'' precipitates are expected to provide effective resistance to dislocation motion. This stage has been found to facilitate high strength retention due to its needle-like, coherent structure. It is thought to inhibit dislocation movement through the slip plane [41]. In the aging processes performed at 300 °C, it was observed that there was a continuous reduction in tensile strength as the duration of the process increased. After 30 min, the strength decreased to 336.09 MPa; after 60 min, it further decreased to 281.39 MPa; and after 90 min, it decreased to 248.41 MPa. These results are consistent with over-aging-related changes in the precipitation state, including precipitate coarsening and changes in precipitate–matrix coherency, both of which are known to influence precipitation-strengthening efficiency [30]. Under aging conditions applied at 400 °C, the effects on tensile strength are much more significantly negative. The tensile strength values obtained at 30, 60, and 90 min intervals are 196.88 MPa, 182.59 MPa, and 174.97 MPa, respectively, showing an approximate 55% decrease compared to the initial strength. At this temperature level, the pronounced strength loss is consistent with a substantial reduction in precipitation-hardening efficiency, which may be associated with extensive precipitate coarsening and/or partial dissolution at elevated temperature.

The strain hardening exponent (n) values obtained for the 6082-T6 aluminum alloy under different post-aging temperature and time conditions are presented in figure 6. In aging tests conducted at 100 °C, n values remained within the range of 0.119–0.122 for three different aging times (30, 60, and 90 min). The limited range of n values indicates that the initial precipitate state inherited from the T6 temper is preserved at this low temperature, with insufficient thermal activation to induce microstructural degradation or significant phase transformations. The relatively stable n values at 100 °C suggest that the strain-hardening response remains close to that of the initial T6 condition. At 200 °C, the range for n was between 0.120 and 0.126, implying that there was no compromise in the mechanical stability of the alloy. It is observed that the hardening behavior significantly differs during the aging

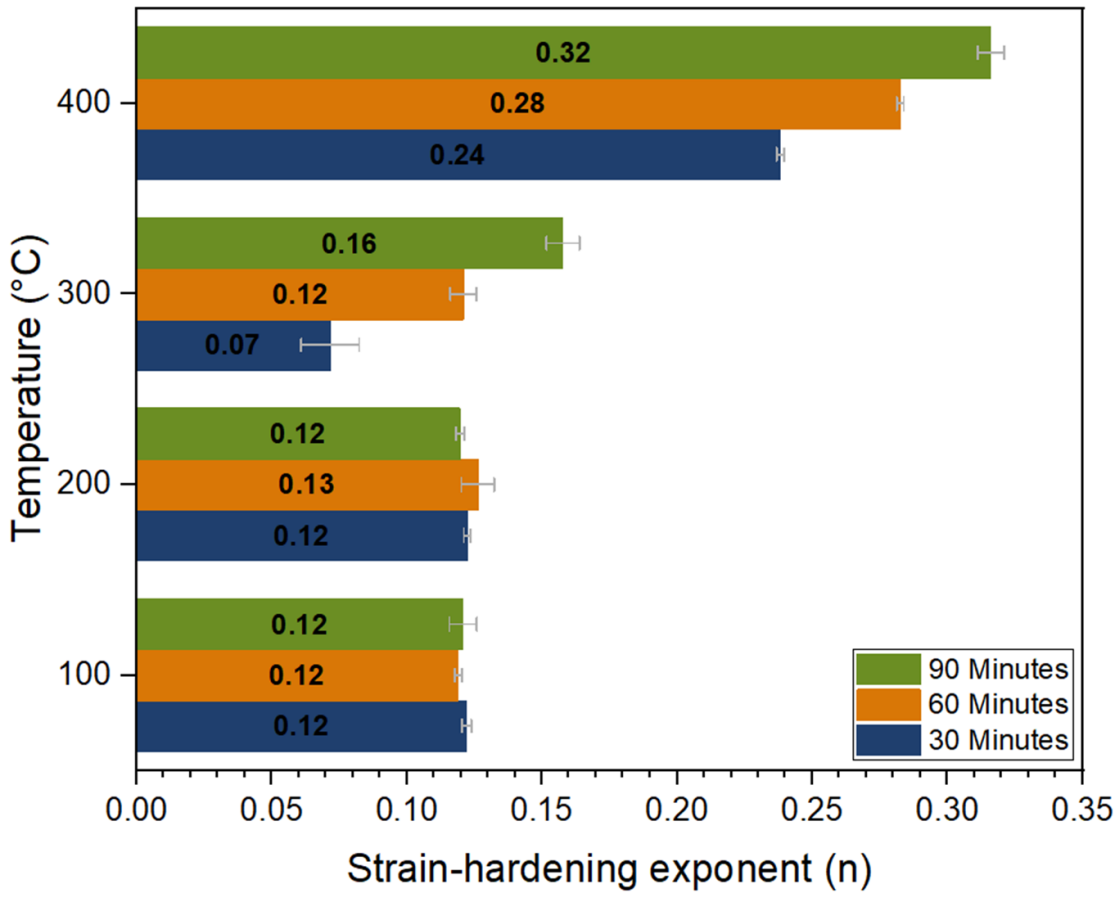


Figure 6. Strain-hardening exponent with post-aging temperature and duration.

process carried out at 300 °C. The fact that the value of n decreased to 0.072 in a 30 min process suggests that the distance between the precipitates widened and the interaction with the matrix weakened. Less resistance to dislocations can lead to a decrease in hardening capacity. However, the increase in *n*from 0.121 to 0.158 at 60 and 90 min, respectively, may be associated with changes in precipitate distribution and increased dislocation accumulation during deformation. The *n* values of 0.238, 0.283, and 0.316 obtained at 400 °C indicate the effect of high temperature. In such cases, the dissolution and coarsening of precipitates along with the inhomogeneous structure can cause strain localization, which can affect the estimated value of *n*. It is thought that, under long-term aging conditions at 400 °C, microstructural instabilities limit deformation propagation, causing the increased n values to reflect strain localization rather than mechanical improvement or enhanced strain-hardening behavior [45].

As demonstrated in figure 7, the measured values of uniform elongation for the 6082-T6 aluminum alloy were determined under various post-aging temperature and time conditions. The uniform strain value of the as-received T6 condition was measured as 14.31%. In the context of aging processes conducted at 100 °C, uniform elongation values of 14.36%, 16%, and 14.45% were obtained under conditions of 30, 60, and 90 min, respectively. The findings demonstrate that matrix ductility is more effectively preserved under lower-temperature aging conditions. This behavior aligns with the minimal precipitation observed at reduced temperatures, facilitating dislocation movement during plastic deformation [46]. Ductility reaches its maximum level at 60 min of aging, which corresponds to 16%. During aging at 200 °C, the uniform elongation levels ranged from 14.81% to 15.90%. The formation of fine and coherent β'' precipitates within this range promotes uniform plastic deformation while maintaining strength [47]. However, a substantial change in the observed phenomenon occurs at the temperature of 300 °C. The measured values in 30, 60, and 90 min treatments have decreased to a range of 8.96%–9.62%. The phenomenon is associated with precipitate development, leading to a loss of coherence and less contact with the matrix. The coarsening of precipitates may lead to a reduction in ductility as a result of stress concentration [48]. However, at 400 °C, a divergent behavioral pattern emerges. As the uniform elongation remains at 11.06% and 12.88% for 30- and 60 min treatments, respectively, it is evident that this value increases to 18.17% with a 90 min treatment. The increase in uniform elongation

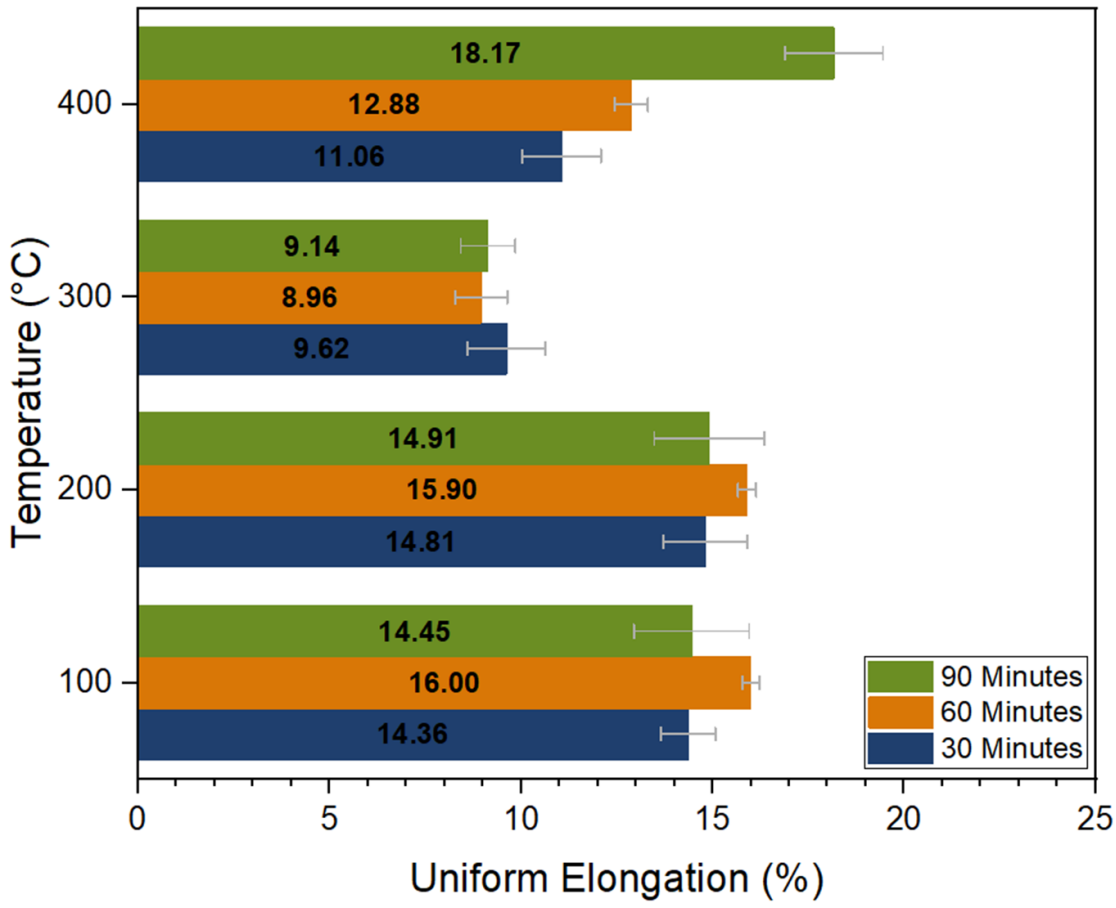


Figure 7. Uniform elongation response under different post-aging conditions.

at 400 °C, particularly after 90 min, is mainly attributed to matrix softening caused by extensive precipitate dissolution/coarsening, despite the severe reduction in strength. This situation may promote a more homogeneous dislocation distribution and continuous plastic flow during deformation [49, 50].

Figure 8 shows the total elongation capacity (%) of the 6082-T6 aluminum alloy under different post-aging temperature and time conditions. The total elongation value for the as-received T6 condition was determined to be 15.73%. In the 100 °C aging processes, the total elongation values obtained were measured as 15.39%, 17.50%, and 15.85% under conditions of 30, 60, and 90 min, respectively. These results indicate that the ductile structure of the matrix is largely preserved at low aging temperatures. Aging processes applied at 200 °C also show similarly high ductility values. The total elongation values obtained for 30, 60, and 90 min treatments were 16.38%, 17.42%, and 16.37%, respectively, indicating that precipitation hardening did not suppress ductility. At 300 °C, a significant decrease in total elongation values was observed, with total elongation values of 11.69%, 11.44%, and 12.44% obtained under conditions of 30, 60, and 90 min, respectively. The simultaneous loss of both strength and ductility at this temperature is a critical finding that cannot be adequately explained by intra-granular precipitate coarsening alone. Instead, this degradation may be associated with grain-boundary effects and heterogeneous microstructural recovery. At elevated temperatures like 300 °C, coarse precipitates tend to nucleate and grow preferentially along grain boundaries, often accompanied by the formation of adjacent precipitate-free zones (PFZs). These softer PFZs, combined with coarse-grain-boundary particles, promote early strain localization, as visually confirmed by our DIC strain maps showing premature necking. Furthermore, as supported by the fractographic analysis (figure 17), these coarse particles act as preferential sites for coarse-particle-controlled void nucleation, leading to the formation of larger, irregularly distributed dimples. Consequently, the localized strain at the grain boundaries rapidly coalesces into macroscopic damage, severely curtailing the macroscopic ductility before significant uniform deformation can occur. This decrease in behavior can occur as a result of the localization of dislocation movements by local barriers and the heterogeneity of plastic deformation [51, 52]. At 400 °C, total elongation increased from 13.93% after 30 min to 20.52% after 90 min. However, this increase should not

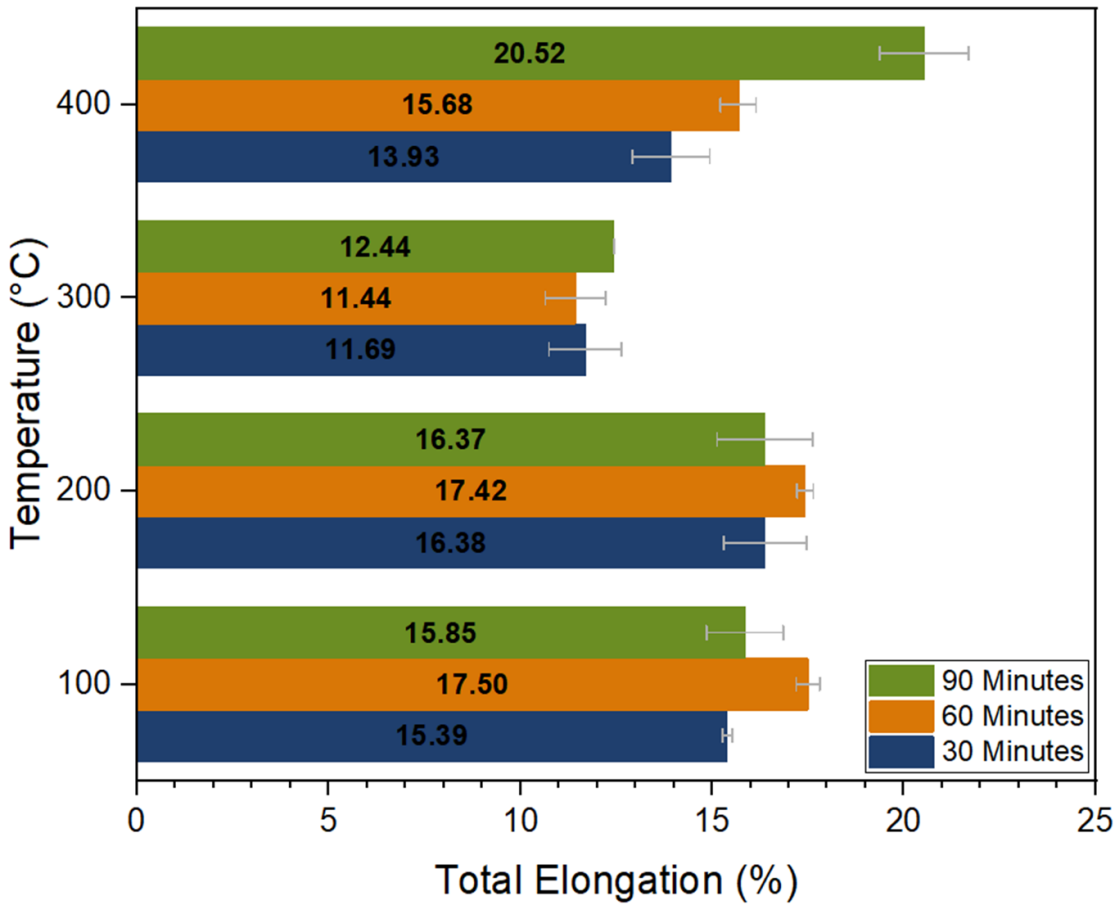


Figure 8. Total elongation behavior of AA6082-T6 after post-aging treatments.

be interpreted as an overall mechanical improvement, because it occurs together with a severe reduction in strength. Instead, the higher elongation at 400 °C, particularly after 90 min, can be attributed to matrix softening caused by extensive precipitate dissolution/coarsening, which promotes easier dislocation motion and more widespread plastic deformation [53].

As shown in figure 9, the energy absorption per unit volume (E_v, MJ m^{-3}) of the 6082-T6 aluminum alloy was calculated under various post-aging temperature and time conditions. *Ev* was determined by numerical integration of the area under the true stress–true strain curve up to fracture, as expressed by: $\mathrm{Ev} = \int_0^{\varepsilon_f} \sigma_{\mathrm{true}}(\varepsilon)\,\mathrm{d}\varepsilon$ where σ_{true} is the true stress and ε_f is the fracture strain. Since stress is expressed in MPa and strain is dimensionless, the calculated *Ev* values are equivalent to MJ m^{-3}. The *Ev* value for the T6 condition was calculated to be 53.34 MJ m^{-3}. Under aging conditions at 100 °C, the *Ev* values for 30, 60, and 90 min treatments were 55.00, 60.71, and 54.96 MJ m^{-3}, respectively. At 200 °C, the *Ev* values were 56.51 MJ m^{-3} for a 30 min treatment, 61.36 MJ m^{-3} for a 60 min treatment, and 56.95 MJ m^{-3} for a 90 min treatment. These values indicate that the energy absorption capacity is maintained compared to the T6 condition and even improves in medium-term aging. This behavior can be explained by the literature-reported precipitate dislocation interactions, particularly those involving β'' precipitates, which contribute to precipitation strengthening and influence plastic deformation [54]. Furthermore, literature studies indicate that suitable aging conditions promote the development of β'' precipitates with high number densities, which contribute significantly to precipitation strengthening in Al–Mg–Si alloys [55, 56]. At 300 °C, the *Ev* values exhibit a decrease. The *Ev* measurements for 30 min, 60 min, and 90 min are 35.99 MJ m^{-3}, 28.78 MJ m^{-3}, and 25.85 MJ m^{-3}, respectively. The notable reduction, evident after prolonged aging, may be associated with over-aging-related microstructural changes; according to the literature, β'-type precipitates and PFZs may develop in 6xxx aluminum alloys and contribute to strain localization and ductile fracture [57]. At a temperature of 400 °C, *Ev* values reached their lowest level. For treatments with durations of 30, 60, and 90 min, the values obtained were 23.12, 23.54, and 28.67 MJ m^{-3}, respectively. Under these conditions, the large-scale dissolution of precipitates and the structural instability of the matrix can hinder effective energy absorption during the deformation process [58].

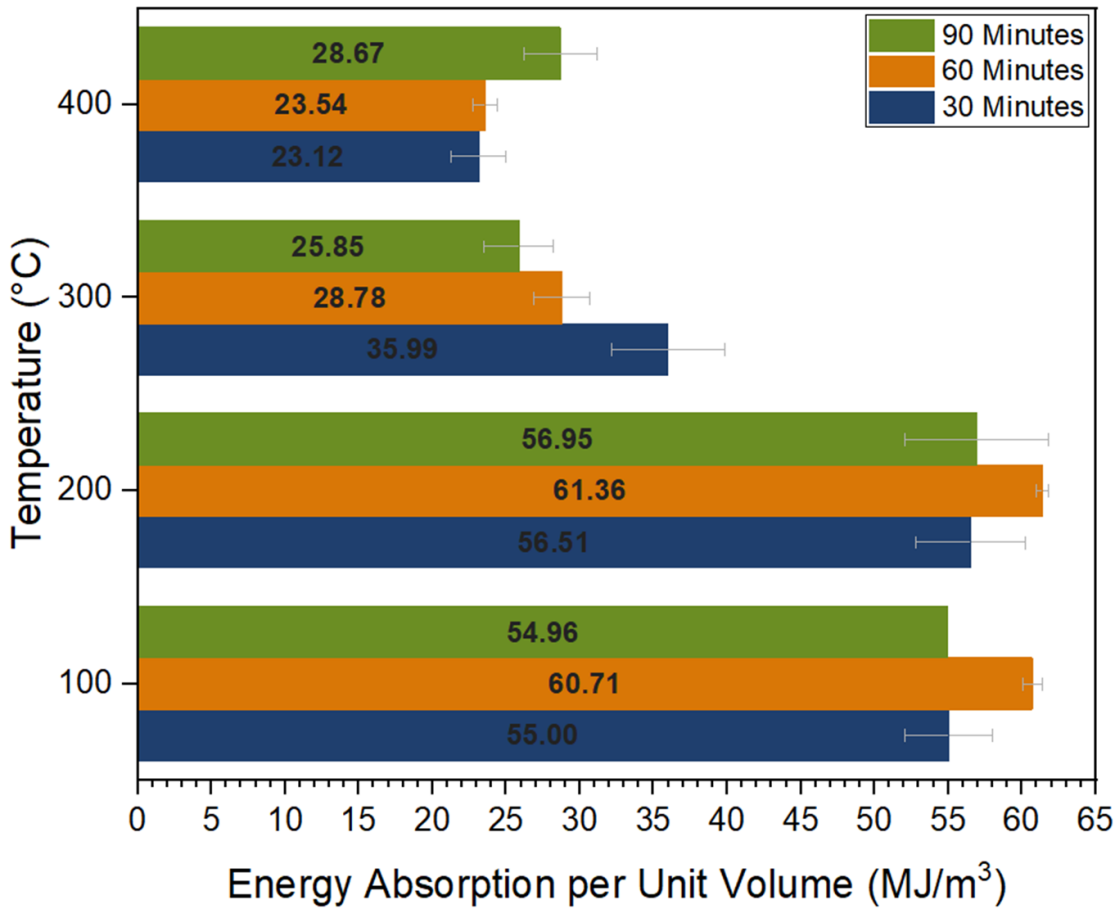


Figure 9. Effect of post-aging temperature and time on energy absorption per unit volume.

Figure 10 illustrates the impact of varying post-aging temperatures and durations on the HV5 of 6082-T6 aluminum alloy. The hardness value in the T6 condition was measured as 108.6 HV. The hardness values obtained after aging processes applied at 100 °C were measured as 111.80 HV at 30 min, 114.00 HV at 60 min, and 115.20 HV at 90 min. These values are consistent with literature-reported precipitation-hardening mechanisms involving GP zones and fine coherent β'' precipitates, which provide effective resistance to dislocation motion. However, in the present study, the hardness values indicate the preservation of the highly effective β'' precipitate network inherited from the initial T6 temper. The lack of thermal degradation at 100 °C ensures that the material retains high resistance to dislocation movement. The slight upward trend in hardness with prolonged time may be attributed to minor secondary precipitation of residual solutes, though the primary strengthening mechanism remains the stable T6 precipitate structure [59]. Aging processes at 200 °C resulted in the highest hardness values. Hardness values of 112.40 HV, 115.60 HV, and 112.20 HV were obtained under 30, 60, and 90 min conditions, respectively. At this temperature, it is understood that the mechanical and hardness responses are consistent with a peak-aged condition associated with fine coherent β'' precipitates, thus maximizing resistance to plastic deformation. Upon aging at 300 °C, a clear decreasing trend in hardness is observed. In a 30 min process, 100.18 HV was measured, in 60 min, 88.92 HV, and in 90 min, 73.98 HV. With increasing aging time, the weakening of the precipitation-strengthening effect may be associated with precipitate coarsening and reduced coherency, consistent with the $\beta'' \rightarrow \beta'$ evolution reported for Al–Mg–Si alloys [31]. Aging processes at 400 °C were the conditions under which hardness was measured at its lowest levels. In the 30, 60, and 90 min applications, the hardness was determined to be 56.96 HV, 51.92 HV, and 48.68 HV, respectively. At this level, the pronounced hardness reduction may be associated with a reduced precipitation-strengthening effect related to changes in precipitate–matrix coherency. Thus, the effectiveness of precipitates as barriers to dislocation motion is reduced, and the material exhibits substantially lower hardness compared with the as-received T6 condition [60].

The XRD patterns presented in figures 11 and 12 show the crystallographic response of the as-received T6 condition and the specimens aged at different temperatures and holding times. The XRD

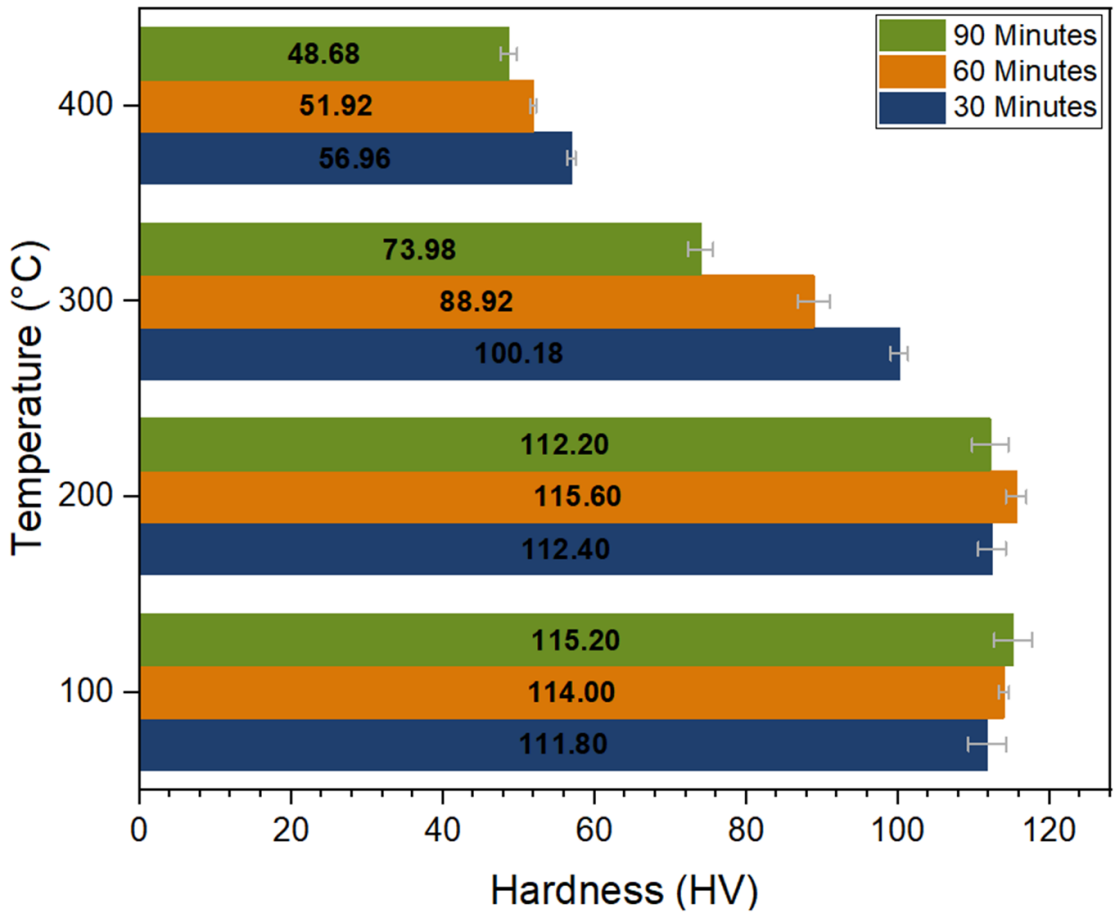


Figure 10. Vickers hardness variation after post-aging at different temperatures and holding times.

analysis of 6082-T6 aluminum alloy (figure 11) shows that the α-Al (FCC) matrix phase is predominantly present in the material's crystal structure. The characteristic peaks identified in the diffractogram are located at $2\theta = 38.4°$ (111), 44.7° (200), 65.1° (220), 78.2° (311), and 82.4° (222) respectively, and correspond to the α-Al phase, consistent with JCPDS card number 04–0787. The lattice parameter calculated using Bragg's law was found to be $a_0 \approx 4.052$ Å, which is consistent with the values reported in the literature for the T6 condition of 6XXX series alloys [20, 61].

As a secondary phase candidate, weak reflections that may be associated with Mg_2Si are expected around ~28.4°, 47.3°, and 56.1° (JCPDS 35–0773). However, under T6 conditions, Mg–Si precipitates are typically nanometric and of low volume fraction; therefore, their direct detection by conventional XRD is limited, and any Mg_2Si-related signals should be interpreted qualitatively rather than as evidence of a dominant bulk Mg_2Si phase. Therefore, the crystalline structure is mainly composed of the α-Al matrix, while possible Mg–Si-based precipitates may contribute to the mechanical response; however, their nanoscale nature limits their direct detection by conventional XRD. Under all conditions, the dominant peaks identified at $2\theta = 38.4°$ (111), 44.7° (200), 65.1° (220), 78.2° (311), and 82.4° (222) correspond to the α-Al (FCC) matrix phase, consistent with the JCPDS 04–0787 reference. The lattice parameter values ($a_0 \approx 4.050$–4.055 Å) show only minor variation across the investigated conditions, suggesting that the α-Al matrix remains largely stable at the scale detectable by XRD. Nevertheless, because peak positions can also be influenced by instrumental factors and residual micro strain, this observation should be interpreted as an indication of limited lattice-level change rather than definitive evidence of zero stress/strain accumulation.

As the aging temperature and time increase, weak Mg_2Si-related reflections (approximately 28.4°, 47.3°, and 56.1°; JCPDS 35–0773) become more noticeable in the XRD patterns. Under low-temperature conditions (100 °C–200 °C) and short holding times, the mechanical and hardness responses are consistent with the presence of fine coherent β'' precipitates. However, because of their nanoscale size and low volume fraction, these precipitates cannot be directly resolved by conventional XRD. At medium and high aging temperatures (300 °C–400 °C), particularly under prolonged holding times, the observed XRD tendencies together with the hardness reduction suggest precipitate growth/coarsening and gradual

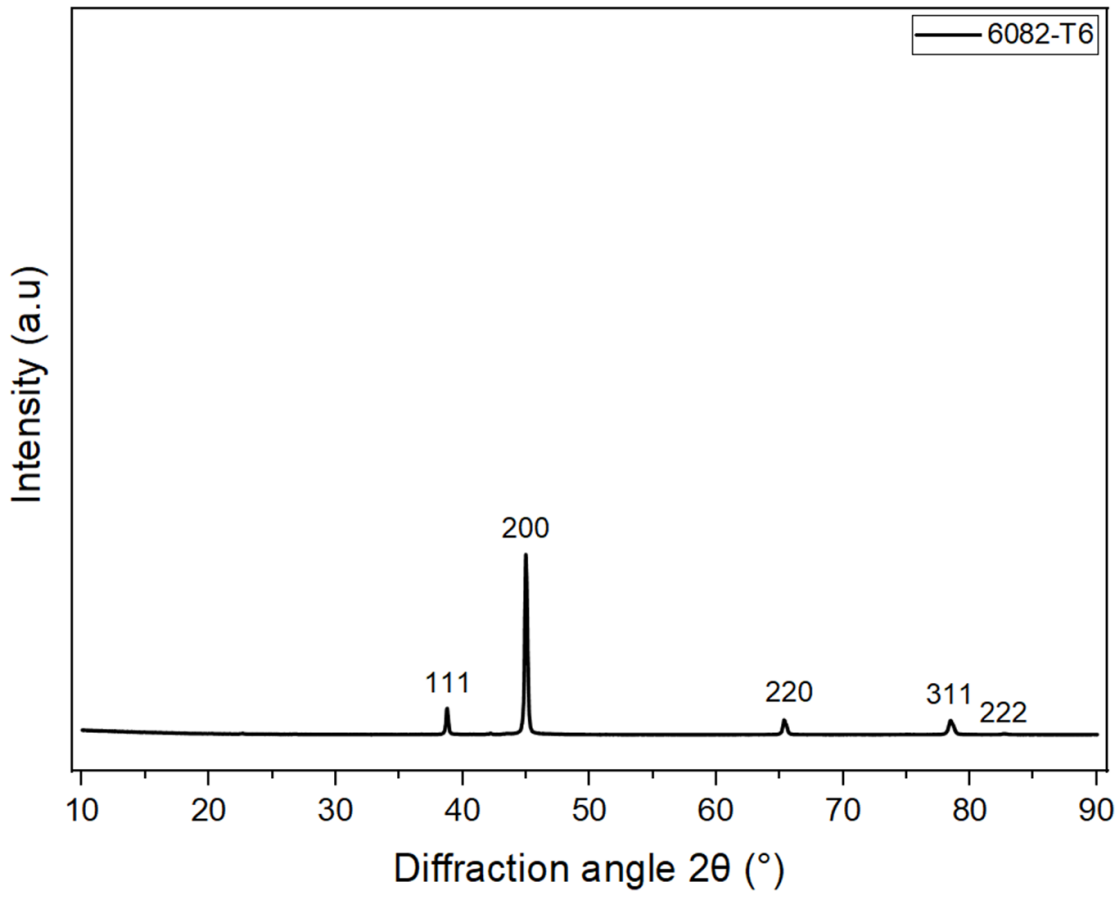


Figure 11. Experimentally measured baseline XRD pattern of the as-received AA6082-T6 alloy.

loss of coherency with the α-Al matrix. Under these conditions, the precipitate population may evolve toward coarser and more stable Mg_2Si-type phases. However, because conventional XRD is not sensitive to nanoscale coherent β''/β' precipitates, these observations should be interpreted qualitatively as evidence of changes in the precipitation state rather than as direct identification of β'', β', or equilibrium β phases. The growth of precipitates and the loss of coherence with the matrix lead to decreases in hardness and yield strength, resulting in the material exhibiting over-aging behavior. Therefore, while low temperatures and short-term aging conditions provide a strengthening effect, high temperatures and long-term conditions lead to a weakening of mechanical properties. The XRD peak broadening behavior was evaluated qualitatively to assess the microstructural evolution induced by different post-aging conditions. As a limitation, the dominance of α-Al reflections and the scarcity of isolated, well-resolved peaks (together with weak Mg_2Si peaks) prevent reliable peak deconvolution/instrumental-broadening correction; hence, Scherrer/Williamson–Hall analyses were not pursued. The observed variations in peak width and intensity may be associated with changes in Mg–Si precipitate populations rather than significant changes in the crystallographic domain size of the α-Al matrix.

The microstructure image of the 6082-T6 alloy is given in figure 13. The changes in the microstructure after post-aging heat treatments are shown in figure 14. The images belong to specimens aged under different temperature (100 °C, 200 °C, 300 °C, and 400 °C) and duration (30, 60, 90 min.) conditions.

Because nanoscale β'' and β' precipitates, as well as distinct microstructural recovery processes, are strictly below the resolution limit of conventional OM, the OM observations in this study are not used to claim direct phase identification. Instead, they are interpreted qualitatively in terms of macroscopic grain-boundary visibility, etching contrast, and coarse intermetallic particles. In the reference (T6) condition, the alloy exhibits equiaxed grains; the strengthening Mg–Si-rich β'' precipitates are too fine to be resolved by conventional OM. Therefore, the matrix appears relatively homogeneous in the presented optical micrographs. This structure serves as the starting reference for post-aging treatments. After the

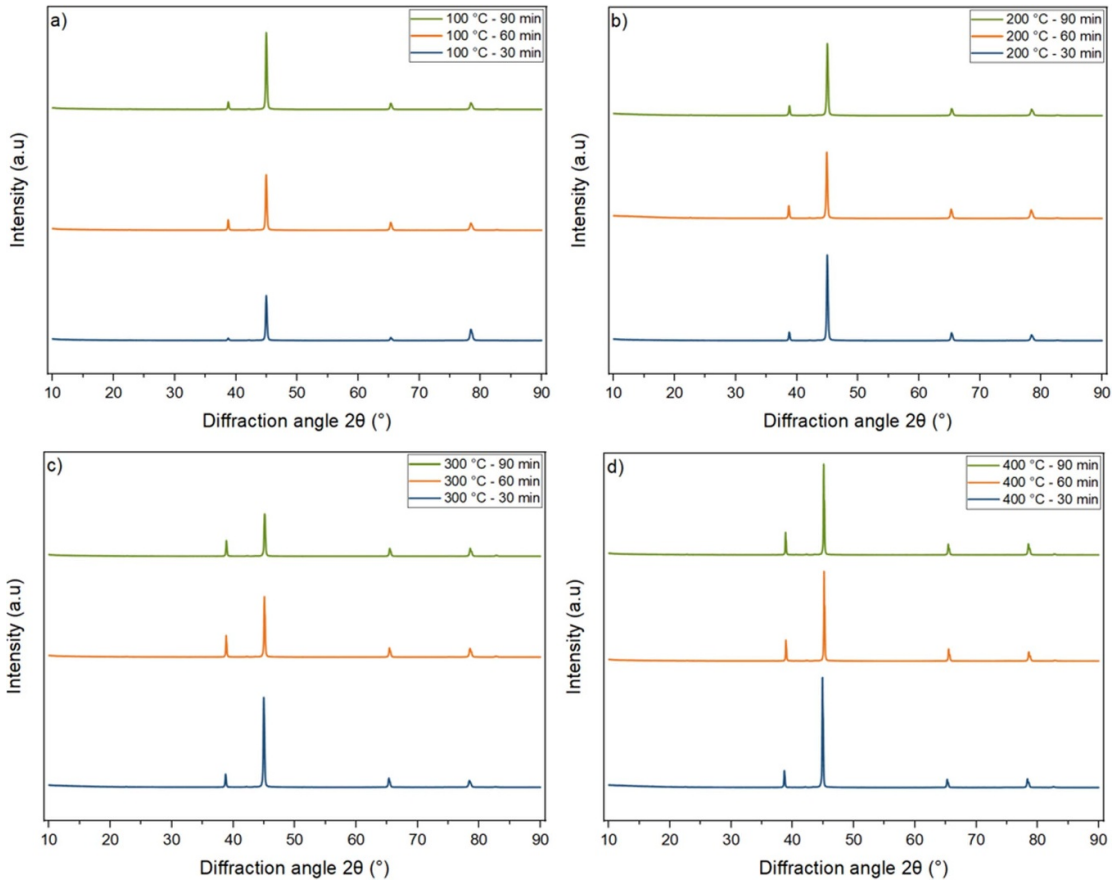


Figure 12. XRD patterns after post-aging treatment a) 100 °C b) 200 °C c) 300 °C d) 400 °C.

aging processes carried out at 100 °C, the microstructure generally remained quite similar to this reference state. Grain boundaries are not clearly visible, and dark, high-contrast intermetallic particles, likely associated with Fe–Mn–Si-containing phases typical of AA6082, are dispersed throughout the matrix. At this temperature, the diffusion rate of Mg and Si atoms is low, so only precursor clusters occur at the atomic scale, and no optically resolvable precipitation is observed. Since the matrix remains homogeneous, there is no coarsening or recrystallization at this stage. The microstructural homogeneities of the specimens were confirmed after they were heat-treated at 200 °C for 30, 60, or 90 min. However, there was a slight enhancement of contrast near the dark phases. These findings are consistent with those observed during the peak aging process, in which the mechanical and hardness responses are consistent with the presence of finely dispersed β'' precipitates. Although these precipitates cannot be resolved by OM, their high density efficiently impedes dislocation movement and augments strength while preserving acceptable ductility. Therefore, while hardness and yield strength increase in mechanical properties, ductility values remain at an acceptable level. From a microstructural perspective, the homogeneous brightness level of the matrix and the still weak appearance of the grain boundaries suggest that the structure remains stable. In specimens aged at 300 °C, the microstructural changes became more pronounced. Grain boundaries have become partially visible, and the size of dark intermetallic phases has increased. This behavior may be attributed to over-aging-related precipitate coarsening and a likely transition from coherent β'' precipitates toward semi-coherent β' phases. As time increases, the microstructural features become more pronounced and exhibit a more heterogeneous distribution within the matrix. The contrast difference between the matrix and grain boundary regions is increasing, and phase separation and local color variations are occurring in some areas. These features indicate the onset of the over-aging phase [62]. Microstructural examination of specimens aged at 400 °C for 30, 60, and 90 min revealed that grain boundaries could be clearly identified, and there was a noticeable contrast between two adjacent grains. These enhanced contrasts are macroscopically consistent with literature reports of microstructural recovery and enhanced coarse precipitation along grain-boundary regions. With increasing temperature and aging time, network-like contrast becomes more pronounced along the grain-boundary regions. This visible morphology is consistent with advanced precipitate coarsening, loss of coherency, and localized microstructural degradation associated with excessive aging at elevated

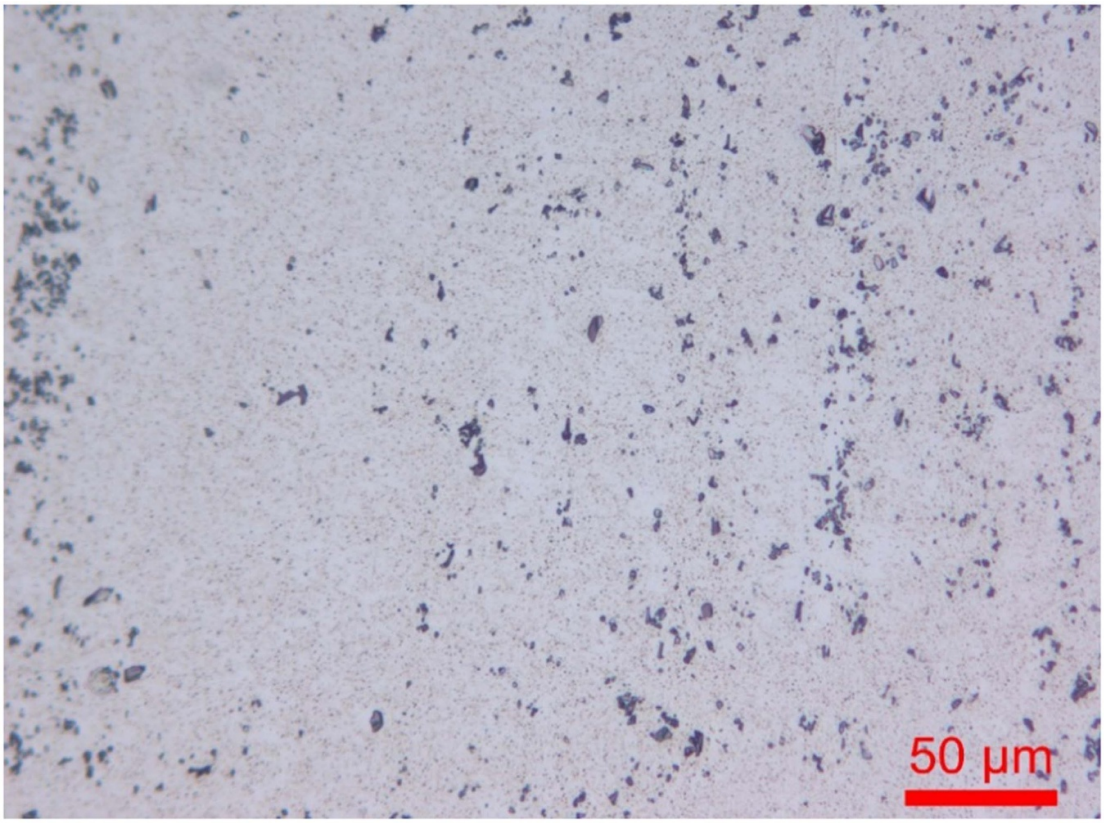


Figure 13. Microstructure of the as-received AA6082-T6 alloy.

temperatures, though definitive confirmation would require high-resolution techniques such as TEM or EBSD.

Dimple diameter histograms obtained from fracture surfaces were analyzed to quantitatively evaluate the effects of post-aging treatments on ductile fracture behavior. In this study, the distributions were characterized using the arithmetic mean dimple diameter (d) and standard deviation (σ) values, calculated from data obtained directly [63].

For each post-aging condition, the average dimple diameter was calculated by dividing the sum of all measured dimple diameters by the total number of observations. This arithmetic mean is expressed by equation (1):

$$\bar{d} = \frac{1}{N}\sum_{i=1}^{N} d_i \tag{1}$$

where $\bar{d}$ represents the average dimple diameter, d_i is the diameter of the ith dimple, and N is the total number of measured dimples.

The standard deviation value, calculated to describe the width of the distribution, is obtained by squaring the deviation of each observation from the mean, summing these deviations, dividing by $(N-1)$, and taking the square root of the result. This calculation is defined by equation (2):

$$\sigma = \sqrt{\frac{1}{N-1}\sum_{i=1}^{N}\left(d_i - \bar{d}\right)^2} \tag{2}$$

For each post-aging condition, at least 100 clearly identifiable dimples were measured from a representative SEM fracture-surface image, and only dimples with distinguishable boundaries were included in the quantitative evaluation. Accordingly, the calculated standard deviation represents the within-image dispersion of dimple sizes rather than specimen-to-specimen variability. The dimple diameter distributions are relatively more concentrated under low temperature and short-term post-aging conditions, with standard deviation values that remain comparable among these conditions. This situation indicates that microvoid nucleation and growth occur more uniformly, and the fracture surface exhibits a ductile

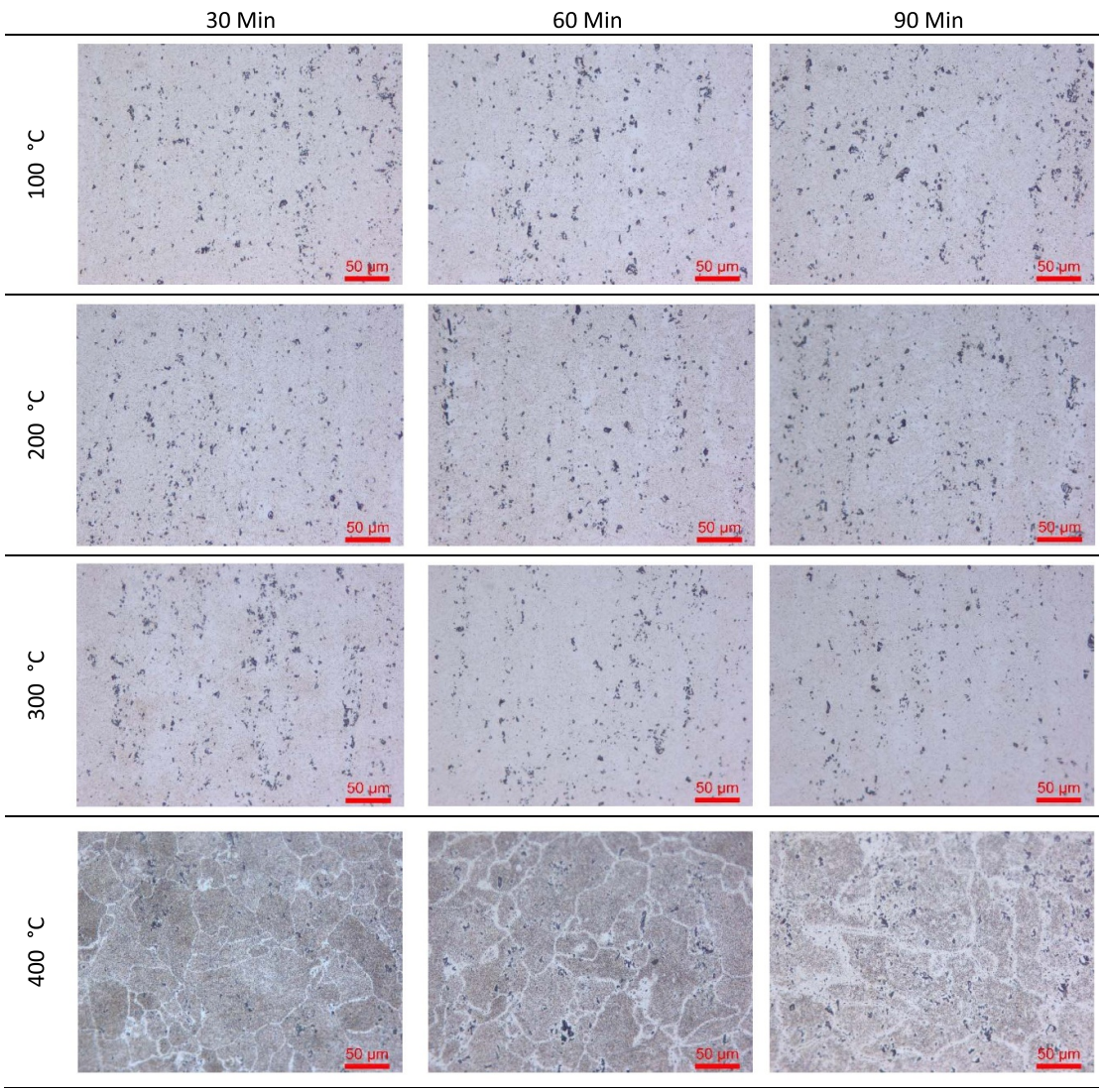


Figure 14. Optical micrographs of AA6082-T6 after post-aging at 100 °C–400 °C for 30, 60, and 90 min.

character. In contrast, a modest increase in the mean dimple diameter and distribution width, together with a clearer reduction in dimple density and the emergence of larger voids in the tail of the distribution, was observed under high-temperature and long-term aging conditions. These increases indicate that dimple formation has become more heterogeneous and the fracture surface has acquired a more irregular morphology, consistent with the overaging-related microstructural changes inferred from the mechanical, hardness, OM, and XRD results.

Figure 15 clearly shows that ductile fracture behavior is dominant on the fracture surface of the as-received 6082-T6 aluminum alloy. The presence of spherical dimples seen in the fractured surface provides evidence for ductile microvoid fracture behavior, which consists of void formation, growth, and coalescence. The lack of cleavages on the fracture surface indicates that significant plastic deformation capability was preserved during the fracture. As illustrated in figure 16, the histogram of dimple sizes indicates an average diameter of 0.857 μm, with a standard deviation of 0.798 µm. The size distribution is particularly concentrated in the 0.3–1.5 μm range, and the presence of larger dimples reaching 3.5–4.0 μm, although few in number, is also noteworthy. This situation indicates that there is some heterogeneity within the microstructure in terms of size and distribution; however, this heterogeneity is not at a level that would suppress the characteristic of ductile fracture.

Figure 17 shows fracture surface images of the 6082-T6 aluminum alloy subjected to different post-aging temperatures and durations. Compared to the fracture morphologies observed after aging processes (100 °C–400 °C, 30–90 min), as-received 6082-T6 alloy stands out as the specimen with the finest dimple structure and the highest microvoid density. Particularly at temperatures of 300 °C and above,

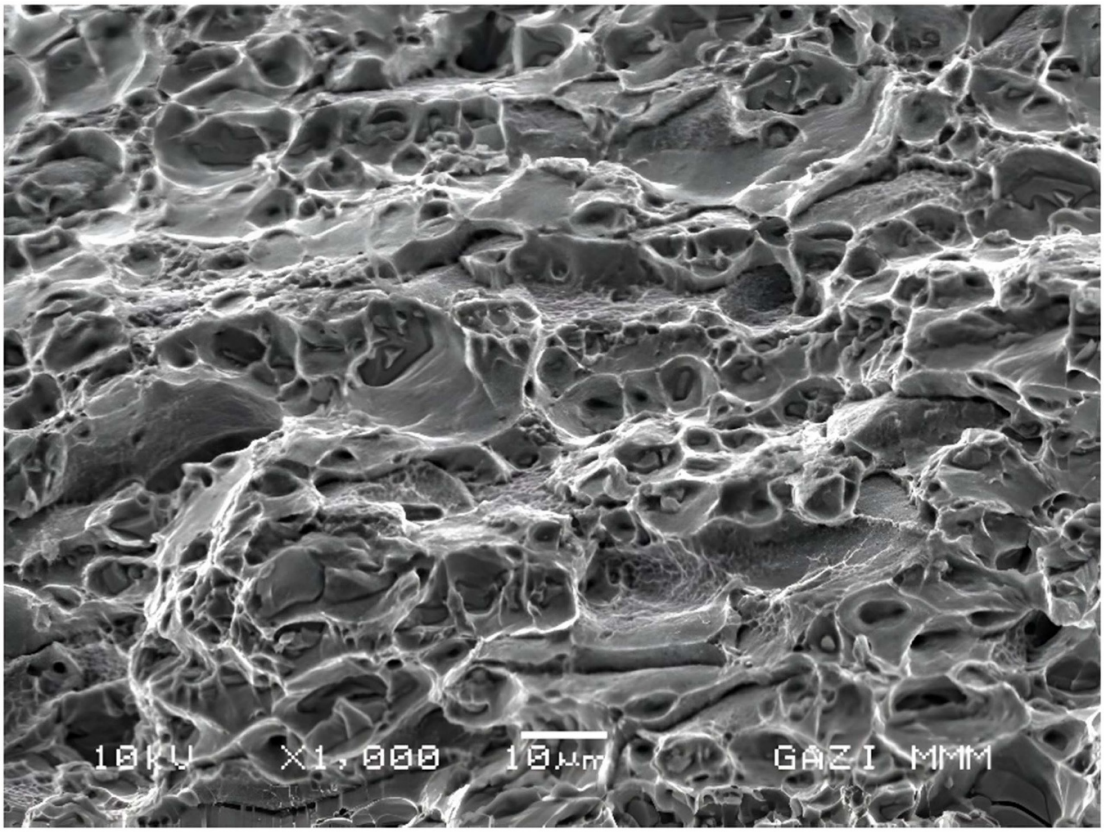


Figure 15. Fracture surface of the as-received 6082-T6 alloy after uniaxial tensile testing.

with aging times of 60 min or longer, the fracture surface tends to exhibit lower dimple density and a more pronounced population of larger voids, indicating increased heterogeneity in microvoid nucleation and coalescence. These changes are consistent with precipitate coarsening/overaging and matrix softening, which promote earlier strain localization. Overall, the fracture morphology remains predominantly ductile. The regions where large dimples are concentrated correspond to areas where void coalescence is accelerated, resulting in a decrease in tensile strength and energy absorption capacity.

The dimple morphology observed on the fracture surface of the 6082-T6 alloy after post-aging processes (100 °C–400 °C, 30–90 min) exhibits noticeable changes with temperature and time, as evaluated by both the average dimple diameter data (figure 18) and the size distribution histograms (figure 19).

In aging processes conducted at 100 °C, the average dimple diameter ranges from 0.883 to 0.965 μm. The largest average diameter (0.965 μm) was measured in the specimen processed for 30 min, while the diameter gradually decreased with increasing processing time. The fact that the standard deviation values remain within a comparable range, such as 0.802–0.857 μm in this range, indicates that precipitate coarsening is limited and the matrix hardness is largely preserved. Therefore, microvoid nucleation likely initiates around coarse intermetallic particles and larger non-shearable precipitates, a well-documented mechanism in 6xxx series alloys [44, 57], limiting premature void coalescence and maintaining a homogeneous ductile morphology. At 200 °C, the average dimple diameters ranged from 0.880 to 0.953 μm, with the maximum value (0.953 μm) obtained particularly at a processing time of 30 min. The observed variation in dimple size may be associated with changes in precipitate dislocation interactions and local plastic deformation around second-phase particles, while the overall mechanical response remains consistent with a precipitation strengthened condition. The standard deviation values remained within the range of 0.805–0.831 μm, indicating a broadly comparable level of dimple-size dispersion. When the temperature reaches 300 °C, the average dimple diameter values are observed to be between 0.888 and 0.951 μm. The highest average diameter (0.951 μm) was obtained after 30 min, followed by a decrease at 60 min and a subsequent increase at 90 min. The standard deviation values ranging from 0.819 to 0.876 μm indicate a relatively broad dimple-size distribution and a more heterogeneous fracture surface at this temperature. Increasing the distance between microvoids reduces the continuity of local plastic deformation and weakens ductile fracture behavior. At 400 °C, the average

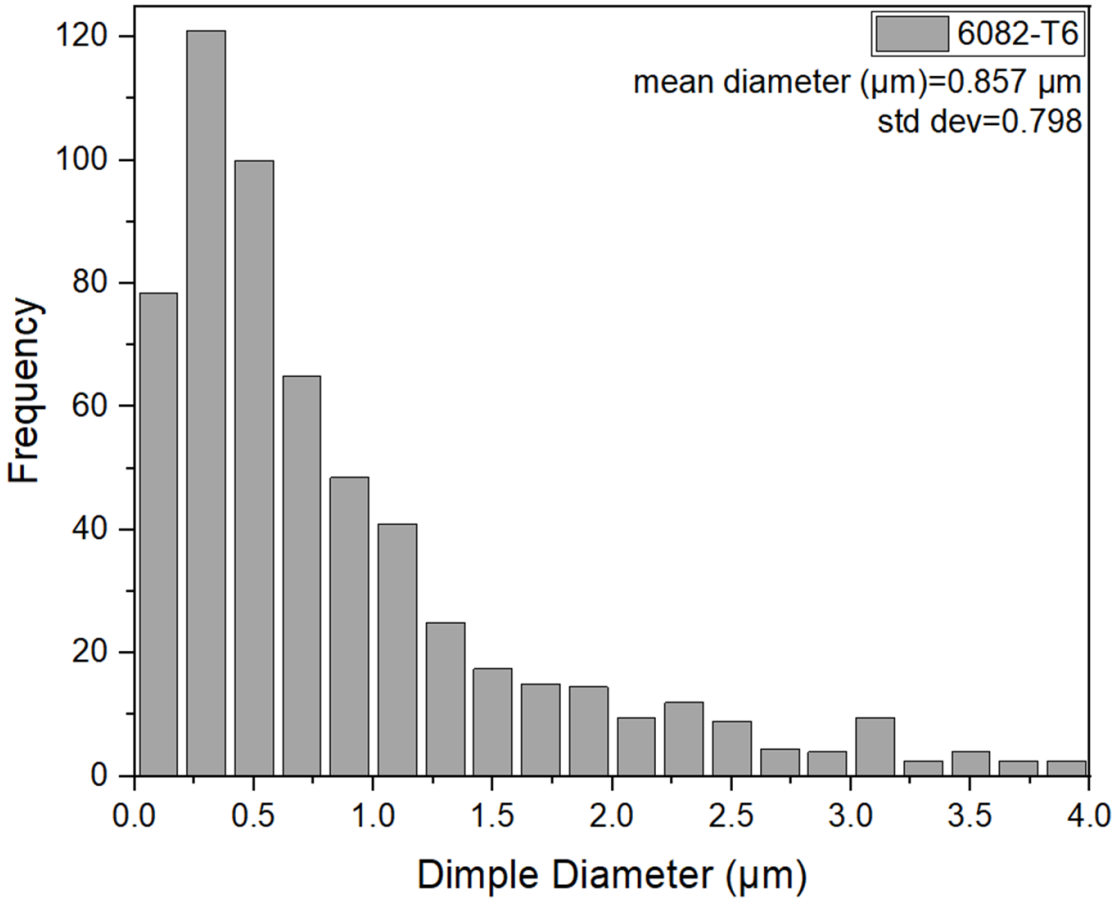


Figure 16. Dimple size histogram of as-received 6082-T6 alloy based on our baseline experimental measurements.

dimple diameters range from 0.884 to 0.974 μm. Specifically, with a 90 min processing time, the highest average diameter value of 0.974 μm was achieved under all conditions. This situation indicates enhanced coarse precipitate formation and matrix softening, promoting heterogeneous void growth and coalescence. Under these conditions, the standard deviations, which reach values as wide as 0.811–0.887 μm, indicate that the fracture process evolved into an irregular, heterogeneous character dominated by large voids.

Low-temperature and short-duration post-aging treatments (100 °C–200 °C, 30–60 min) maintain homogeneous ductile fracture behavior, exhibiting dimple characteristics similar to the T6 condition; high-temperature and long-duration treatments (300 °C–400 °C, 60–90 min) lead to heterogeneous fracture surfaces characterized by large and widely distributed dimple morphology. In this case, it is believed that post-aging parameters directly affect the fracture behavior through the loss of precipitate and matrix hardness. Therefore, high temperatures and long durations should be limited when considering the material's mechanical performance.

4. Conclusion

The effects of post-aging temperature and time on the mechanical response, microstructure, and fracture behavior of AA6082-T6 were examined using combined experimental characterization and DIC analysis. The findings of this study are provided below.

- The most favorable post-aging condition was determined to be 200 °C for 60 min. A favorable strength–ductility balance was achieved under these conditions. Under these conditions, the yield strength was measured as 288.3 MPa, tensile strength as 400.6 MPa, uniform elongation as 15.9%, total elongation as 17.4%, hardness as 115.6 HV, and energy absorption per unit volume as 61.36 MJ m^{-3}. These values indicate that effective precipitation hardening is achieved while maintaining relatively homogeneous deformation.

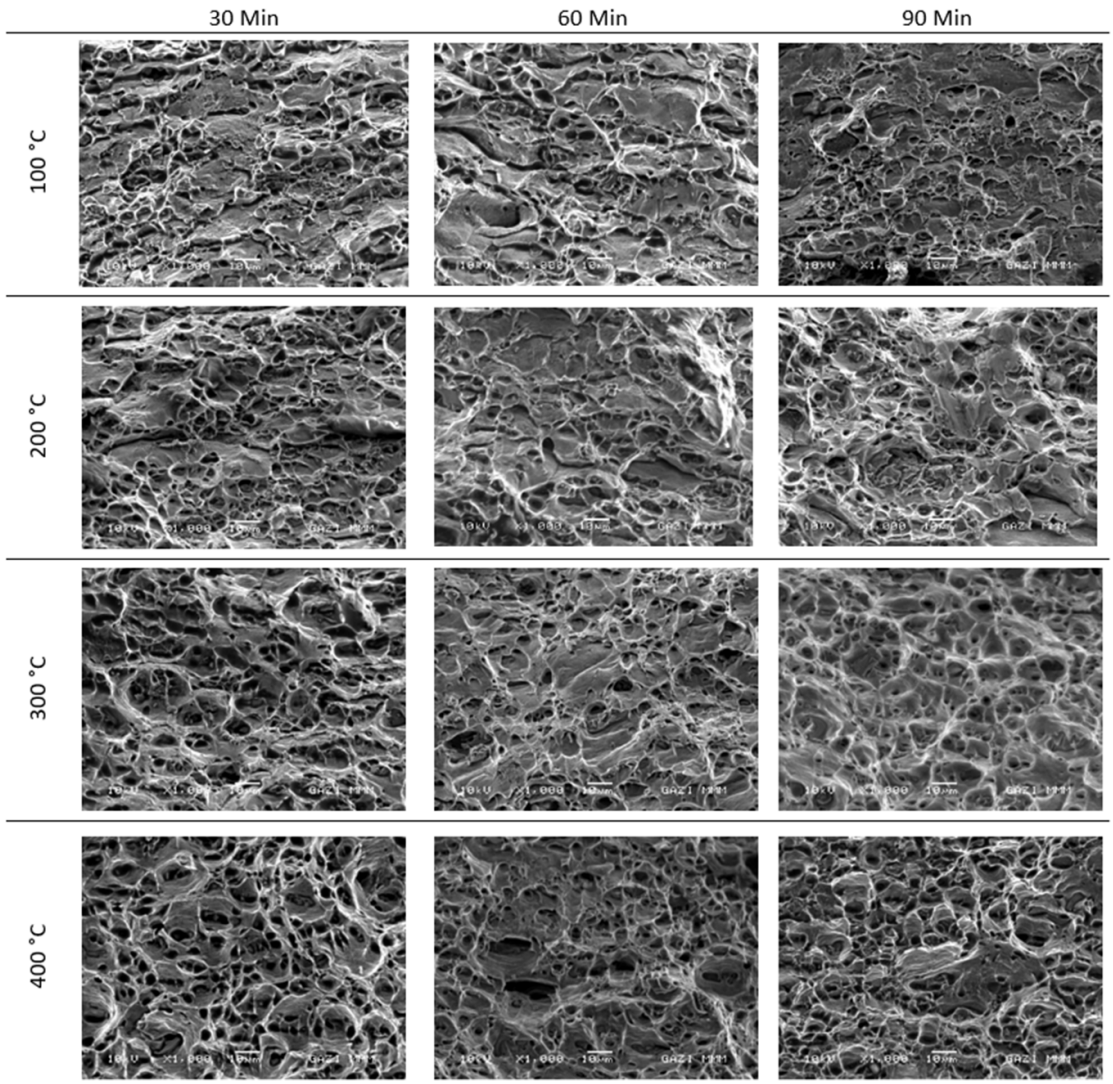


Figure 17. Fracture surfaces of AA6082-T6 after post-aging at 100 °C–400 °C for 30–90 min.

- Aging at 200 °C for 60 min corresponds to a peak-aged condition in terms of precipitation hardening. In addition, increasing temperature and prolonged holding times, particularly at 300 °C–400 °C, promote over-aging effects.
- The combined hardness, tensile, XRD, and OM observations suggest a progressive transition from a fine precipitate-strengthened condition toward a coarser overaged microstructural state with increasing temperature. At 200 °C, the mechanical and hardness responses are consistent with a peak-aged condition associated with fine coherent β'' precipitates. In the range of 300 °C–400 °C, precipitate coarsening and microstructural heterogeneity along grain boundary regions became more pronounced.
- At 300 °C–400 °C, the mechanical response, hardness reduction, and XRD tendencies suggest progressive precipitate coarsening and a transition toward more stable Mg_2Si-type precipitate structures. At 300 °C, precipitate coarsening and loss of coherency reduce the material's ability to accommodate plastic deformation, leading to reduced ductility and earlier strain localization. At 400 °C, however, pronounced matrix softening leads to increased elongation, particularly after 90 min, despite the severe reduction in strength. However, the fracture behavior remains predominantly ductile, characterized by microvoid coalescence, and cleavage features are not observed.
- Fracture surface examinations revealed a fine and relatively uniform dimple morphology at 200 °C, whereas 300 °C–400 °C treatments produced more heterogeneous dimple distributions with a greater occurrence of larger voids, indicating an enhanced tendency for void coalescence.

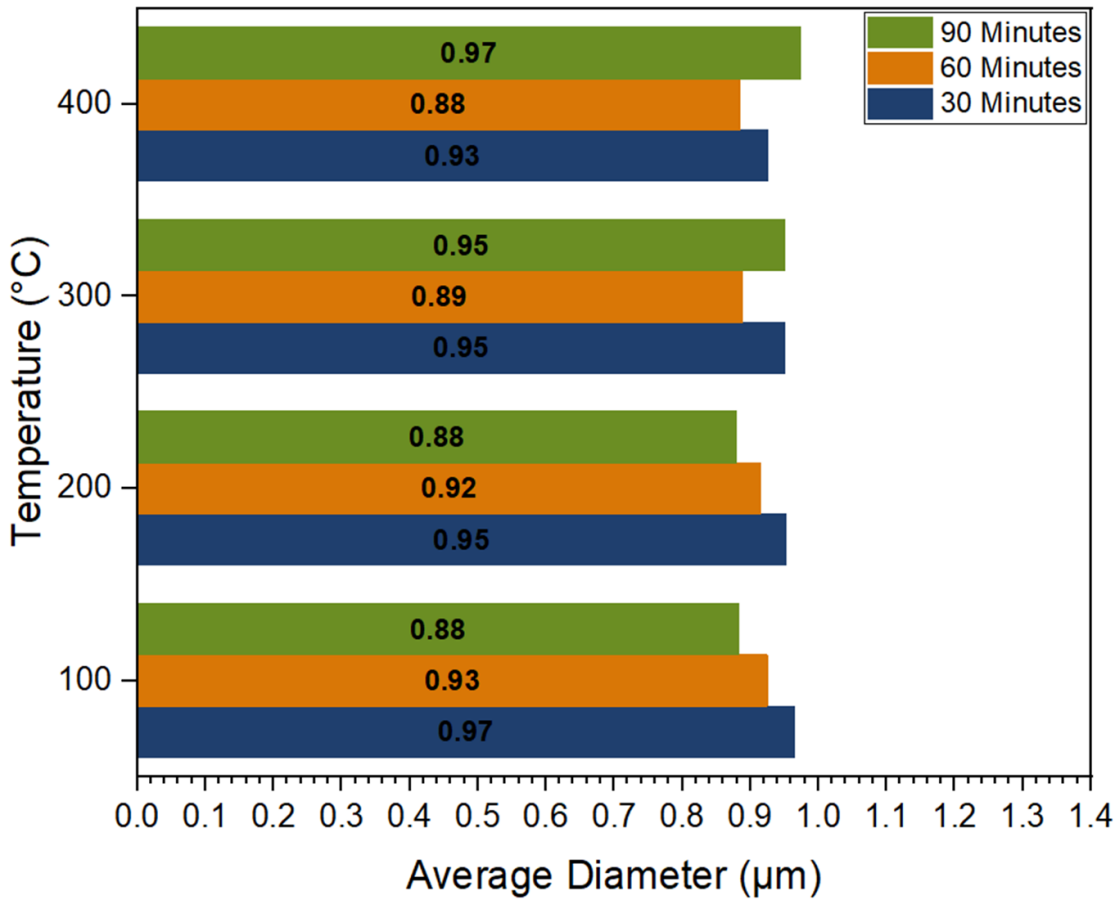


Figure 18. Average dimple diameter as a function of post-aging temperature and time.

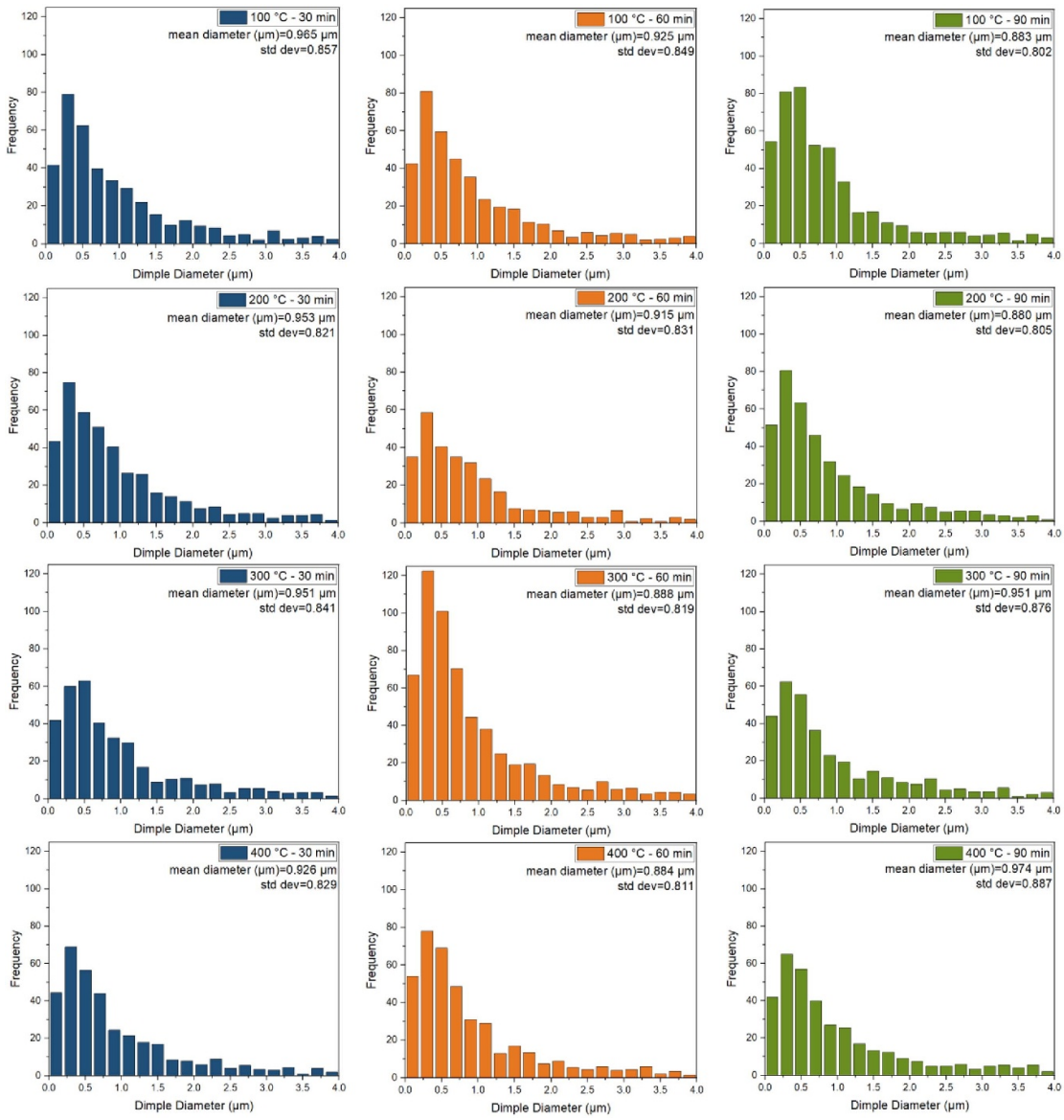


Figure 19. Dimple size histograms of AA6082-T6 after post-aging at 100 °C–400 °C for 30–90 min.

Acknowledgment

The authors gratefully acknowledge the Department of Engineering Science at the University of Oxford for providing access to its DIC testing facilities, which supported the experimental phase of this research.

Data availability statement

The data that support the findings of this study are available upon reasonable request from the authors.

The cost of preparing and organizing the dataset for deposition in a public repository would require additional time and resources, not available to the authors at the time of publication. The data supporting this study will remain available from the authors upon reasonable request.

Funding

This research received no financial support from any funding agency, institution, or organization.

Conflict of interest

The authors declare there is no conflict of interest.

Author contributions

Mehmet Okan Kabakçı 0000-0003-0086-9294
Data curation (equal), Formal analysis (equal), Investigation (equal), Methodology (equal), Visualization (equal), Writing – original draft (equal)

Onur Cavusoglu 0000-0002-7239-3902
Conceptualization (equal), Data curation (equal), Formal analysis (equal), Validation (equal), Writing – original draft (equal), Writing – review & editing (equal)

Ömer Şahin 0000-0002-2446-2512
Data curation (equal), Investigation (equal), Methodology (equal), Visualization (equal), Writing – original draft (equal)

Oktay Cavusoglu 0000-0002-2826-1814
Data curation (equal), Formal analysis (equal), Investigation (equal), Methodology (equal), Writing – original draft (equal)

Şaziye Efendioğlu Ünal
Data curation (equal), Investigation (equal), Writing – original draft (equal)

Anıl Ozdemir 0000-0001-6563-5144
Conceptualization (equal), Formal analysis (equal), Supervision (equal), Visualization (equal), Writing – review & editing (equal)

References

[1] Gao Y C *et al* 2024 Research progress, application and development of high performance 6000 series aluminum alloys for new energy vehicles *J. Mater. Res. Technol.* **32** 1868–900
[2] Thavasilingam K, Senthil K A, Sakthimurugan D and Giridharan K 2025 Aluminum alloys for aircraft structures *Aerospace Materials: Novel Technologies and Practical Applications* (Elsevier) pp 385–404
[3] Çavuşoğlu O, Sürücü H İ, Toros S and Alkan M 2020 Thickness dependent yielding behavior and formability of AA6082-T6 alloy: experimental observation and modeling *Int. J. Adv. Manuf. Technol.* **106** 4083–91
[4] Jacob A, Maheshwari S, Siddiquee A N and Gangil N 2018 Improvements in strength and microstructural behaviour of friction stir welded 7475 aluminium alloy using in-process cooling *Mater. Res. Express* **5** 076518
[5] Nunes H, Emadinia O, Soares R, Vieira M F and Reis A 2023 Adding value to secondary aluminum casting alloys: a review on trends and achievements *Materials* **16** 895
[6] Ben Moses R, Ajith Raj R, Vijay Judges I and Barath Srinivas P 2024 Casting and microstructural characterization of high-performance 2000 series aluminum alloy for aerospace applications *J. Phys.: Conf. Ser.* **2837** 012103
[7] Liu F, Zhu F, Yang W, Wang Q and Tu Y 2025 Improved mechanical properties of 2024 aluminum alloys by electric pulse assisted rolling and subsequent aging *Mater. Des.* **254** 114053
[8] Wang Y, Shi L, Su R, Liu T and Li G 2024 Effect of intermittent non-isothermal aging on the microstructure and properties of Al–Zn–Mg–Cu alloy *Mater. Chem. Phys.* **328** 129946
[9] Sharath B N, Pradeep D G and Madhu K S 2024 A review on the potential impact of age hardening on aluminium alloys and hybrid composites for engineering applications *Prog. Eng. Sci.* **1** 100013
[10] Yang Y L, Chung T F, Ali M S, Dilshad and Zhao P 2023 The influence of creep ageing on the hardening behavior and microstructure of 7050 aluminum alloy *Metals* **13** 196
[11] Perrin T *et al* 2025 Investigation of the high thermal ageing resistance of the 2219 aluminium alloy *Mater. Des.* **256** 114373
[12] Ren X, Liang W, Zhang Y, Zhang Z, Wang Q, Zhao X, Bai S and Meng M 2025 Microstructural evolution and mechanical properties of an Al-10Zn-3Mg-2.5Cu alloy processed by stress-aging coupled artificial aging *Mater. Des.* **260** 114984
[13] Dewangan S and Kulkarni A R *et al* 2026 Microstructural changes and tensile fractography of Al-6061 after solutionizing and aging *Mater. Res. Express* **13** 126501
[14] Li K, Liu K, Su R, Li G and Qu Y 2025 The effect of multi-stage aging treatment on the microstructure and properties of 7075 aluminum alloy *J. Alloys Compd.* **1032** 181143
[15] Tan E, Ovali I, Yildiz R and Dispinar D 2025 Simultaneous improvement in strength and ductility of AA6082 by interrupted aging *Eur. J. Mech. A* **114** 105753
[16] Zhou Y, Cao Y, Yang L, Huang G and Feng Y 2026 Effects of aging temperature on microstructure and mechanical properties in cold-rolled 2024 aluminum alloy *Mater. Chem. Phys.* **350** 131905
[17] Chen X, Zhang X, Zhang W, Xu Z, Wang H, Song H and Xue T 2021 Effect of ageing on the structure and properties of continuously-cast and rolled sheet of aluminum alloy 6061 *Met. Sci. Heat Treat.* **63** 304–11
[18] Yin Q, Jiang L, Guo F and Wang Z 2023 Microstructure and properties of 6 series aluminum alloy under different aging treatment systems *Medziagotyra* **29** 439–44

[19] Görtan M O and Yüksel B 2023 Dependency of mechanical properties on artificial aging conditions for EN AW 6082 aluminum alloy *Metall. Res. Technol.* **120** 204
[20] Hu Z, Zheng J, Pang Q, Sun Q and Zhao N 2023 Influence of strain rates and aging time on microstructure and hardness of integrally compressed 6082 aluminum alloy *J. Mater. Res. Technol.* **27** 826–38
[21] Liu Y, Pan Q, Liu B, Yu Q, Li G and Pan D 2022 Effect of aging treatments on fatigue properties of 6005A aluminum alloy containing Sc *Int. J. Fatigue* **163** 107103
[22] Sui Z, Liu L, Chang Z, Yan X, Zhang Y, Li Y, Zhang Y and Yang M 2025 Effect of aging treatment on microstructure and mechanical properties of as-extruded AA6063 aluminum alloy *J. Mater. Eng. Perform.* **34** 5506–16
[23] Xia E, Ye T, Qiu S, Liu J, Luo J, Sun L and Wu Y 2024 Mechanical properties and microstructural evolution of 6082 aluminum alloy with different heat treatment methods *Coatings* **14** 602
[24] Okayasu M and Okawa M 2022 Effect of artificial aging on the mechanical and fatigue properties of the hot-stamped 6022 aluminum alloy *J. Mater. Eng. Perform.* **31** 6386–94
[25] Arslankaya S 2020 Estimating the effects of heat treatment on aluminum alloy with artificial neural networks *Emerg. Mater. Res.* **9** 540–9
[26] Chen L, Yuan S, Kong D, Zhao G, He Y and Zhang C 2019 Influence of aging treatment on the microstructure, mechanical properties and anisotropy of hot extruded Al-Mg-Si plate *Mater. Des.* **182** 107999
[27] Österreicher J A, Tunes M A, Grabner F, Arnoldt A, Kremmer T, Pogatscher S and Schlögl C M 2020 Warm-forming of pre-aged Al-Zn-Mg-Cu alloy sheet *Mater. Des.* **193** 108837
[28] Gong B S *et al* 2023 Investigation on the fatigue behavior of 7075 aluminum alloy at different aging states *Int. J. Fatigue* **175** 107817
[29] Xia E, Ye T, Wang L, Qiu S, Tian Y, Wu C, Luo J and Wu Y 2024 Tensile behavior and microstructure of the 6082 alloy sheet with high-temperature aging treatments *Coatings* **14** 963
[30] Cui A, Wang X and Cui Y 2024 Multiscale modelling of precipitation hardening: a review *J. Mater. Sci. Mater. Theory* **8** 13
[31] Zheng Y-y, Luo B-h, Xie W and Li W 2023 Microstructure evolution and precipitation behavior of Al-Mg-Si alloy during initial aging *China Foundry* **20** 57–62
[32] Bayerlein B, Schilling M, von Hartrott P and Waitelonis J 2024 Semantic integration of diverse data in materials science: assessing Orowan strengthening *Sci. Data* **11** 434
[33] Li R, Takata N, Suzuki A, Kobashi M, Okada Y and Furukawa Y 2021 Precipitation hardening at elevated temperatures above 400 °C and subsequent natural age hardening of commercial Al–Si–Cu alloy *Materials* **14** 7155
[34] Wu Y, Chen Z, Le W, Zhang H, Song W and Yang Z 2024 Optimization of high-temperature mechanical properties of aluminum alloys through exclusive precipitation of T-phase *J. Mater. Res. Technol.* **33** 3144–54
[35] Li C, Marioara C D, Hatzoglou C, Andersen S J, Holmestad R and Li Y 2025 Chemical composition dependent atom clustering during natural aging in Al-Mg-Si alloys *Scr. Mater.* **257** 116474
[36] Jiang G D, Cai Y H, Qiu C, Zhang W W and Zhang D T 2022 Effect of over-aging on the microstructure, mechanical properties and crashing performance of thin-walled Al-Mg-Si-Cu alloy profiles *J. Mater. Res. Technol.* **21** 3074–85
[37] Li Q, Qin J, Jiang D, Yi D and Wang B 2022 Precipitate coarsening and mechanical properties in 6082 aluminium alloy during long-term thermal exposure *J. Alloys Compd.* **909** 164819
[38] Saito G, Sano Y, Mizuno K, Torigoe S, Takata K, Okajima T and Muto S 2025 Precipitation behavior during low-temperature aging in Al–Mg–Si alloy using STEM-EDS intensity correlograms *Mater. Sci. Eng. A* **923** 147686
[39] Chemin A E A *et al* 2019 Characterization of phases, tensile properties, and fracture toughness in aircraft-grade aluminum alloys *Mater. Des. Process. Commun.* **1** e79
[40] Zheng Y, Luo B, Bai Z and He C 2019 Evolution of the initial precipitation and strengthening mechanism of Al-Mg-Si alloys *JOM* **71** 4737–45
[41] Mao H *et al* 2020 β" needle-shape precipitate formation in Al-Mg-Si alloy: phase field simulation and experimental verification *Comput. Mater. Sci* **184** 109878
[42] Hu Y and Curtin W A 2021 Modeling peak-aged precipitate strengthening in Al–Mg–Si alloys *J. Mech. Phys. Solids* **151** 104378
[43] Yang L, Bai D, Wang D, Liu C, Yang S and Huang G 2023 Effect of aging temperature on microstructure and corrosion behavior of 6082 aluminum alloy *Mater. Today Commun.* **36** 106583
[44] Madanat M, Liu M and Banhart J 2018 Reversion of natural ageing in Al-Mg-Si alloys *Acta Mater.* **159** 163–72
[45] Cerri E and Ghio E 2024 On the work-hardening behaviour of the additively manufactured Al-Si-Mg alloys: composite-like versus networked microstructure *Materialia* **38** 102282
[46] Wang Z, Chen M, Jiang H, Li H and Li S 2020 Effect of artificial ageing on strength and ductility of an Al-Cu-Mg-Mn alloy subjected to solutionizing and room-temperature rolling *Mater. Charact.* **165** 110383
[47] Ringdalen I, Wenner S, Friis J and Marian J 2017 Dislocation dynamics study of precipitate hardening in Al-Mg-Si alloys with input from experimental characterization *MRS Commun.* **7** 626–33
[48] Ren J, Hong Z, Zhou Q, Xu X and Yin S 2024 Effect of aging treatment temperature on microstructure and properties of Al-Si-Mg cast aluminum alloy *J. Mater. Eng. Perform.* **33** 13284–92
[49] Afifi M A, Wang Y C and Langdon T G 2020 Effect of dynamic plastic deformation on the microstructure and mechanical properties of an Al–Zn–Mg alloy *Mater. Sci. Eng. A* **784** 139287
[50] Mohammed S, Gupta S, Li D, Zeng X and Chen D 2020 Cyclic deformation behavior of a heat-treated die-cast Al-Mg-Si-based aluminum alloy *Materials* **13** 4115
[51] Yang M *et al* 2021 Shearing and rotation of β″ and β′ precipitates in an Al-Mg-Si alloy under tensile deformation: *in-situ* and ex-situ studies *Acta Mater.* **220** 117310
[52] Rakhmonov J, Liu K, Rometsch P, Parson N and Chen X-G 2021 Effects of Al(MnFe)Si dispersoids with different sizes and number densities on microstructure and ambient/elevated-temperature mechanical properties of extruded Al–Mg–Si AA6082 alloys with varying Mn content *J. Alloys Compd.* **861** 157937
[53] Choi K, Lee S and Bae D 2024 Natural and artificial aging effects on the deformation behaviors of Al–Mg–Zn alloy sheets *Materials* **17** 4478
[54] Kong S, Liu Q and Zhang Z 2023 Mechanism on material strengthening of metastable precipitate and edge dislocation in Al–Mg–Si Alloy *Phys. Status Solidi B* **260** 2200478
[55] Chen Y *et al* 2023 Effect of the solid solution and aging treatment on the mechanical properties and microstructure of a novel Al-Mg-Si Alloy *Materials* **16** 7036

[56] Yang M et al 2020 Quantified contribution of β″ and β′ precipitates to the strengthening of an aged Al–Mg–Si alloy *Mater. Sci. Eng. A* **774** 138776
[57] Ringdalen I G, Jensen I J T, Marioara C D and Friis J 2021 The role of grain boundary precipitates during intergranular fracture in 6xxx series aluminium alloys *Metals* **11** 894
[58] Zuo J, Hou L, Shu X, Peng W, Yin A and Zhang J 2020 Investigation of deformation induced precipitation and the related microstructure evolution of Al-Zn-Mg-Cu alloy *Mater. Res. Express* **7** 106529
[59] Maeda T, Kaneko K, Namba T, Koshino Y, Sato Y, Teranishi R and Aruga Y 2018 Structural and compositional study of precipitates in under-aged Cu-added Al-Mg-Si alloy *Sci. Rep.* **8** 16629
[60] Tavakkoli V, Boltynjuk E, Scherer T, Mazilkin A, Ivanisenko Y, Ungar T and Kübel C 2024 Precipitate-mediated enhancement of mechanical and electrical properties in HPTE-processed Al–Mg–Si alloy *Mater. Sci. Eng. A* **906** 146556
[61] Huang F, Zhang D, Deng Y, Cheng Z, Sun Q, Hu Z and Hua L 2025 Microstructure evolution behaviors and mechanical properties of 6082–0.2Zr-0.3Er alloy during the pre-hardened hot forming process *Materials* **18** 616
[62] Meyruey G, Massardier V, Lefebvre W and Perez M 2018 Over-ageing of an Al-Mg-Si alloy with silicon excess *Mater. Sci. Eng. A* **730** 92–105
[63] Tioguem F, N'guyen F, Mazière M, Tankoua F, Galtier A and Gourgues Lorenzon A F 2020 Advanced quantification of the carbide spacing and correlation with dimple size in a high-strength medium carbon martensitic steel *Mater. Charact.* **167** 110531